J. Fluid Mech. (2009), *vol.* 625, *pp.* 321–351.
doi:10.1017/S0022112008005715 Printed in the United Kingdom

Linear and nonlinear processes in two-dimensional mixing layer dynamics and sound radiation

LAWRENCE C. CHEUNG[1]† AND SANJIVA K. LELE[1,2]

[1]Department of Mechanical Engineering, Stanford University, Stanford, CA 94305-3030, USA
[2]Department of Aeronautics and Astronautics, Stanford University, Stanford, CA 94305-3030, USA

(Received 23 June 2008 and in revised form 10 December 2008)

In this study, we consider the effects of linear and nonlinear instability waves on the near-field dynamics and aeroacoustics of two-dimensional laminar compressible mixing layers. Through a combination of direct computations, linear and nonlinear stability calculations, we demonstrate the significant role of nonlinear mechanisms in accurately describing the behaviour of instability waves. In turn, these processes have a major impact on sound generation mechanisms such as Mach wave radiation and vortex pairing sound. Our simulations show that the mean flow correction, which is required in order to accurately describe the dynamics of large-scale vortical structures, is intrinsically tied to the nonlinear modal interactions and accurate prediction of saturation amplitudes of instability waves. In addition, nonlinear interactions are largely responsible for the excitation and development of higher harmonics in the flow which contribute to the acoustic radiation. Two flow regimes are considered: In supersonic shear layers, where the far-field sound is determined by the instability wave solution at sufficiently high Mach numbers, it is shown that these nonlinear effects directly impact the Mach wave radiation. In subsonic shear layers, correctly capturing the near-field vortical structures and the interactions of the subharmonic and fundamental modes become critical due to the vortex pairing sound generation process. In this regime, a method is proposed to combine the instability wave solution with the Lilley–Goldstein acoustic analogy in order to predict far-field sound.

1. Introduction

The major role that discrete instability waves play in determining the acoustic radiation from mixing layers and jets has prompted a need to understand the fundamental linear and nonlinear processes that affect their behaviour. Several major advances in aeroacoustics, such as the work of Tam & Morris (1980), Tam & Burton (1984*a*, *b*) and Goldstein & Leib (2005), have been predicated on the ability of linear instability wave theory to predict sound from supersonic shear layers. However, few studies thus far have addressed the relative importance of nonlinear instability wave interactions and mean flow interactions to the sound generation process. In this paper, we contrast the sound radiation mechanisms from two-dimensional supersonic and subsonic laminar mixing layers forced by linear and nonlinear instability waves. Using the nonlinear Parabolized Stability Equations (PSE) and direct calculations,

† Email address for correspondence: l.cheung@imperial.ac.uk

we demonstrate the importance of nonlinear interactions in accurately predicting the spatial evolution of these mixing layers and, as a result, the far-field radiated sound.

This work seeks to answer several open questions concerning the behaviour of instability waves and their link to acoustic radiation. For instance, the importance of modal interactions in capturing the overall shear layer dynamics and the resulting acoustic radiation has not been addressed directly in the literature. Also, in cases of Mach wave radiation from mixing layers and jets, questions often arise regarding the necessity of including nonlinear effects, or whether a simple accounting of the mean flow spreading is sufficient. To address these questions, we consider the behaviour of discrete instability waves which are at the origin of two sound generation processes in mixing layers: Mach wave radiation and vortex sound. Through careful analysis we can isolate the various effects due to nonlinear modal interactions, mean flow corrections and inlet conditions and also determine their relative influence on the radiated sound levels in each case.

1.1. *Prior work*

Several previous theoretical studies are directly relevant to the present study and are worth noting. From the early work of Crighton & Gaster (1976), Tam & Morris (1980) and Tam & Burton (1984*a*, *b*), to the more recent studies by Avital, Sandham & Luo (1998*a*, *b*), Wu (2005) and Goldstein & Leib (2005), these theories have formed the basis for explaining the dynamics of linear instability waves, and established their role in the aeroacoustics of jets and mixing layers. For instance, in the work of Crighton & Gaster (1976), they developed methods to model the growth of instability waves in a slowly diverging jet flow through the multiple scales method. This was also used in Tam & Morris (1980) and Tam & Burton (1984*a*, *b*), where they found that the linear stability solution could be extended into the far field to capture the acoustic radiation from high-speed supersonic mixing layers.

At the same time, however, several important studies also indicated that interactions between instability waves were responsible for the generation of large vortical structures that appear in mixing layers when harmonically forced. From experimental evidence gathered by Brown & Roshko (1974) and Winant & Browand (1974), the work of Ho & Huang (1982) and Laufer & Yen (1983) noted that the interaction between the subharmonic and fundamental modes leads to the vortex pairing process and plays a significant role in determining the acoustic source location. In the review by Tam (1995), the link between large vortical structures, instability waves and sound emission is further discussed in the context of supersonic jet noise.

More recent work has focused attention on the nonlinear developmentof instability waves and more complex models of instability wave based sound generation in mixing layers. For instance, wave packet models were employed by Avital *et al.* (1998*a*) to study Mach wave radiation for time-developing mixing layers. Their analysis indicated that the most dominant mode for acoustic radiation was a two-dimensional mode which evolved from the nonlinear development of the mixing layer. Additional work regarding the nonlinear evolution of supersonic instability waves in Mach wave radiation was carried out by Wu (2005). Using a matched asymptotic expansion combined with the multiple scales method, he accounted for the nonlinear spatial evolution of the instability wave through nonlinear terms arising from the critical layer. The influence of nonlinear mechanisms in sound generation has also been examined by Sandham, Morfey & Hu (2006) in their study of convecting vortex packets. Their formulation was based on a pair of linearized Euler equations and restricted the nonlinear interactions to the source terms of the Lilley–Goldstein acoustic analogy.

A comprehensive study has not yet been undertaken to determine the role of nonlinear instability wave interactions in capturing the dynamics of vortical structures, nor their importance in determining the level and directivity of acoustic radiation. At finite amplitudes, the growth of the instability waves affects the evolution of the mean flow, which can in turn trigger the growth (or dampening) of higher harmonics in the flow. This phenomena naturally raises questions of whether the initial amplitudes and inlet conditions for instability waves have a sizable effect on the downstream evolution of the shear layer and the resulting acoustic radiation. One can also ask whether the eventual saturation of instability waves is mainly due to the effects of mean flow spreading, or if the transfer of energy between modes plays a more significant role. Some questions still remain as to whether the presence of large vortical structures in shear layer and jet flows can be accounted for independently of the instability wave dynamics, or if the development of such structures is intrinsically tied to the interactions of the instability waves. Previous work by Hultgren (1992) sought to answer these questions through the use of matched asymptotic analysis on weakly non-parallel incompressible mixing layers, but a fully nonlinear study has yet to be undertaken.

A natural approach to investigating these questions is to use the Nonlinear Parabolized Stability Equations (NPSE). Since its development by Herbert & Bertolotti (1987) and Bertolotti, Herbert & Spalart (1992) in the study of boundary layer transition, the PSE has been used in many relevant studies of aeroacoustic and fundamental mixing layer problems. For instance, Balakumar (1994, 1998) and Yen & Messersmith (1998) used linear PSE to calculate the instability wave behaviour for Mach 2.1 jets, and more complex linear and nonlinear PSE calculations were also carried out by Malik & Chang (2000). In their study of the structure and stability of compressible reacting mixing layers, Day, Mansour & Reynolds (2001) also used the technique to examine mixing effectiveness.

NPSE can accommodate the effects of nonlinear mode interactions, non-parallel flow and finite amplitude disturbances. It therefore extends beyond linear instability wave methods and more accurately models the near-field evolution and the far-field aeroacoustics of the mixing layer. Furthermore, the ability of PSE to probe each of the nonlinear effects in isolation or in a combined manner can yield tremendous physical insight into the processes underlying the mixing layer dynamics and sound radiation. For instance, one can investigate the effects of multiple mode interactions either alone, or in conjunction with the mean flow correction.

Although the general shear layer problem includes complex three-dimensional fluid motions arising from a broadband spectrum of forcing, the current study focuses on nonlinear effects between discrete instability waves leading to the creation of large two-dimensional roller structures in the flow and their implications on the subsequent sound generation. While many previous DNS investigations (Sandham & Reynolds 1991; Rogers & Moser 1992) have shown that the three-dimensional evolution of the mixing layer eventually leads to the growth of streamwise rib vortices and spanwise 'kinking' of the rollers, our objective is to gain a fundamental understanding of the two-dimensional processes first, before attacking the complete three-dimensional problem. While the formulation's assumptions limit the method to slowly evolving convectively unstable flows, the capabilities of the PSE are well suited for the scope of this paper's objectives.

To date, few studies have examined the link between the near-field dynamics of nonlinear instability waves with the radiated acoustic field. In Mach wave radiation, the instability wave is directly coupled to the acoustic field, but in

vortex sound generation, an additional nonlinear mechanism is responsible for the acoustic radiation. The creation of sound sources through the nonlinear interaction of instability waves can be analysed through the acoustic analogy method (Lighthill 1952; Phillips 1960; Lilley 1974), and may capture the sound generation process more completely than a pure instability wave theory. Recent advances by Goldstein (2001, 2003, 2005) have led to the development of a 'generalized acoustic analogy', and a method based on filtering in the wavenumber frequency domain was proposed to better understand the 'true' sources of sound. The generalized acoustic analogy has been used by Goldstein & Leib (2005) to attack the problem of instability waves in a non-parallel base flow, but remains restricted to linear processes.

1.2. *Outline*

The primary objective of this study is to address several unanswered questions regarding the linear and nonlinear behaviour of instability waves and their relationship to sound generation in mixing layers. Using a combination of direct computation, linear and nonlinear stability methods, the importance of nonlinear interactions and mean flow corrections to the shear layer dynamics will be illustrated. Three two-dimensional mixing layers, one supersonic and two subsonic, are examined in detail, and two different mechanisms for sound generation – Mach wave radiation and vortex pairing sound – are discussed. In each case, the coupling between the instability waves' near-field hydrodynamics and their radiated far field sound will be examined. In instances where instability wave theory is not expected to provide a complete description of the acoustic radiation, we show how the formulation can be extended using Lilley's acoustic analogy.

The basic problem description and computational details are provided in § 2. The shear layer dynamics and the acoustic radiation characteristics of a typical supersonic and subsonic mixing layers are compared and contrasted in § 3. In § 4, the mixing layer results from linear and nonlinear theory are presented, followed by a detailed discussion of the results for the subsonic mixing layer. Finally, the combined instability wave acoustic analogy technique is shown in § 6 before the conclusion.

2. Methodology

2.1. *Problem description*

The primary focus of this investigation is on the aeroacoustics of two-dimensional laminar compressible mixing layers. An upper speed stream with velocity U_1 overlies the lower speed stream U_2 and the resulting shear causes the mixing layer to develop downstream in the x direction, as represented schematically in figure 1. Conceptually, we divide the domain into a near-field region, where the hydrodynamic motions are dominant, and a far-field region, where the acoustic behaviour is to be determined. In addition, the mixing layer is artificially excited by particular instability waves that are imposed at the inlet location. These inlet instability waves for all calculations were obtained by solving the parallel flow linear stability problem defined by the Rayleigh equation (A 8). The fundamental frequency of the instability waves ω_0 is chosen based upon the most unstable frequency at the inlet of the mixing layer. An instability wave corresponding to the subharmonic frequency $\omega_0/2$ was also included in the subsonic mixing layer case where vortex pairing was to be studied.

This method of artificial excitation generally leads to the development of highly organized periodic vortex structures as the mixing layer evolves downstream. Although this artificial forcing limits a broadband spectrum from developing and precludes

Simulations	M_1	M_2	$Re_{\Delta U}$	St_0	U_c/a_1	$M_{r,1}$	$M_{r,2}$
M29M1	2.9	1.0	1283	0.0419	1.95	0.762	1.138
M25M15	2.5	1.5	3000	0.230	2.00	0.509	0.491
M050M025	0.50	0.25	250	0.201	0.375	0.128	0.122

TABLE 1. Flow conditions for the mixing layer computations. The Reynolds number is calculated as $Re_{\Delta U} = \rho_1(U_1 - U_2)\delta_0/\mu_1$.

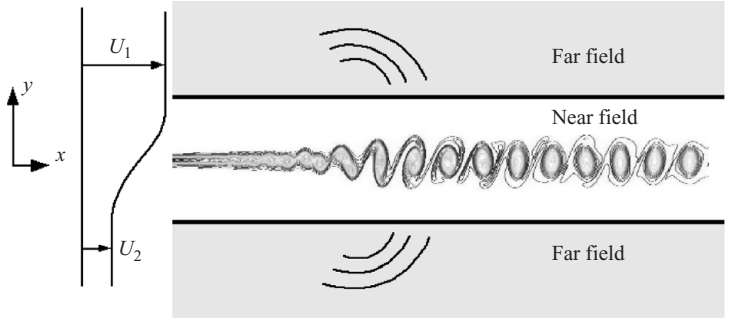

FIGURE 1. Schematic representation of two-dimensional compressible forced mixing layer.

the more complicated turbulent motions of realistic shear flows, it does allow us to investigate the sound generated by specific instability modes and examine the interactions between different modes. Oblique modes were also excluded from the forcing in order to focus on two-dimensional nonlinear interactions and their effects. While the oblique modes tend to be more unstable under higher speed conditions, the influence of three-dimensional structures on sound generation first requires a detailed understanding of the mechanisms of sound radiation from two-dimensional structures.

In table 1, the relevant parameters for three compressible two-dimensional shear layers are given. Both subsonic and supersonic shear layers are included, and they can be characterized based on the convective velocity U_c (Papamoschou & Roshko 1988) and relative phase velocity $M_{r,i}$, as defined by

$$U_c = \frac{a_2 U_1 + a_1 U_2}{a_1 + a_2}, \qquad M_{r,i} = \frac{|\omega/Re\{\alpha\} - U_i|}{a_i},$$

where $i = 1$, 2, and α and ω are the wavenumber and temporal frequency of the primary instability mode, respectively. The speed of sound in the upper and lower streams is denoted by a_1 and a_2, respectively, and $\mathrm{Re}\{\bullet\}$ denotes the real part of the argument. In this study, mixing layers are classified as subsonic if $M_{r,i} < 1$ in both streams, and as supersonic otherwise. In all of the tabulated cases, the temperature ratio between the upper and lower streams was set to $T_2/T_1 = 1$, the Reynolds number $Re_{\Delta U}$ was based on the velocity difference $\Delta U = U_1 - U_2$, initial vorticity thickness δ_0 and upper stream density ρ_1 and μ_1. The Strouhal number of the forced fundamental frequency was defined by $St_0 = \omega_0\delta_0/(2\pi\Delta U)$. The parameter $M_{r,i}$ indicated the general acoustic radiation characteristics of the instability wave into the upper ($i = 1$) and lower stream ($i = 2$) of the mixing layer. In cases where $M_{r,i} > 1$, the instability wave is capable of radiating directly into the corresponding stream in the form of Mach waves, while cases of $M_{r,i} < 1$ suggest that a different mechanism of sound radiation

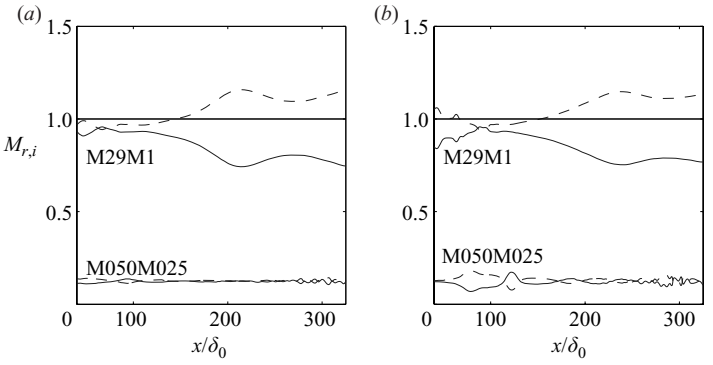

FIGURE 2. The phase speeds $M_{r,1}$ (——) and $M_{r,2}$ (— —) for the forced instability modes. (*a*) The fundamental mode of M29M1 and subharmonic mode of M050M025. (*b*) The first harmonic of M29M1 and fundamental mode of M050M025.

is responsible. In the subsonic mixing layers M25M15 and M050M025, $M_{r,i}$ stated in the table corresponds to the fundamental mode at the inlet. The variation of $M_{r,i}$ with downstream distance for these flows is shown in figure 2. For the supersonic mixing layer M29M1, $M_{r,i}$ is given for the first harmonic, which is the mode initially radiating at the inlet. Results from these shear layers, and simplified models of their behaviour, will be presented in subsequent sections.

2.2. *Computational models*

The behaviour of the instability waves in two-dimensional compressible laminar mixing layers can be determined through the direct computation of the governing Navier–Stokes equations (2.1*a*)–(2.1*d*) for the density ρ, velocities u_i, temperature T, pressure P and dissipation function Φ. Details regarding the simulations, including the numerical methodology and boundary conditions used in the code, are discussed in Appendix A 1.

$$\frac{\partial \rho}{\partial t} + \frac{\partial}{\partial x_i}(\rho u_i) = 0, \tag{2.1a}$$

$$\rho\left(\frac{\partial u_i}{\partial t} + u_j \frac{\partial u_i}{\partial x_j}\right) = -\frac{\partial P}{\partial x_i} + \frac{1}{Re}\frac{\partial}{\partial x_j}\tau_{ij}, \tag{2.1b}$$

$$\rho\left(\frac{\partial T}{\partial t} + u_j \frac{\partial T}{\partial x_j}\right) = \frac{\gamma}{Re\,Pr}\left(\frac{\partial}{\partial x_j}\mu\frac{\partial T}{\partial x_j}\right) - \gamma P\left(\frac{\partial u_j}{\partial x_j}\right) + \frac{1}{Re}\Phi, \tag{2.1c}$$

$$P = \frac{\gamma - 1}{\gamma}\rho T. \tag{2.1d}$$

In conjunction with the direct computations, an instability wave model was also used to probe the nonlinear interactions between modes. Using $\boldsymbol{\phi} = [\rho\, u_1\, u_2\, T]^{\mathrm{T}}$ as the vector of flow variables, this model represented the discrete instability waves in terms of spatially evolving, finite amplitude modes $\hat{\boldsymbol{\phi}}_m(x, y)$ in a slowly developing mean flow. Through the use of the parabolizing approximations (A 5)–(A 6), the nonlinear evolution equation (2.2) can be used to track the behaviour of the instability waves given the nonlinear interaction term $\mathscr{F}_m$ and amplitude factor $\mathscr{A}_m$ defined in

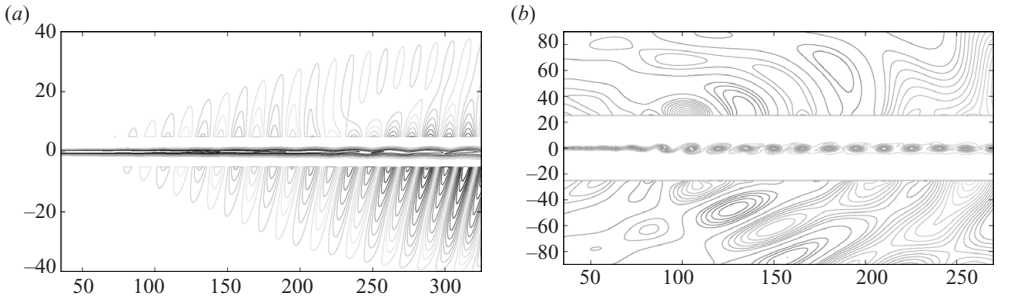

FIGURE 3. Real part of the far-field pressure $\hat{P}_1(x, y)$, superimposed on the instantaneous near-field spanwise vorticity, for the (*a*) M29M1 and (*b*) M050M025 mixing layers. Pressure contour levels: (*a*) -3.5×10^{-2} to 3.5×10^{-2} in steps of 3.5×10^{-3}, (*b*) -5×10^{-6} to 5×10^{-6} in steps of 5×10^{-7}.

Appendix A 2.

$$\mathscr{L}_m\{\hat{\boldsymbol{\phi}}_m\} = \frac{\mathscr{F}_m}{\mathscr{A}_m}. \tag{2.2}$$

In some subsonic shear layers, this model was used to compute the source terms in Lilley's acoustic analogy (Lilley 1974) in order to capture the sound radiated from vortex pairing processes. Further discussion of the combined PSE-acoustic analogy method is found in Appendix A 2, along with a more comprehensive description of the PSE implementation and methodology.

3. Direct computations

The differences between Mach wave radiation and vortex sound generation can be best illustrated by examining the direct calculations of the supersonic (M29M1) and subsonic (M050M025) mixing layers. In the supersonic mixing layer, the instability mode forcing at the inlet triggers a direct response in the far-field pressure, resulting in strong Mach wave radiation downstream (figure 3*a*). This is evident in situations where the phase speed of the instability mode is supersonic relative to the free stream, such as for the fundamental and first harmonic modes. For the first harmonic, $M_{r,2}$ is supersonic at the inlet (figure 2), and thus the mode can radiate into the lower stream immediately, while the fundamental mode is initially subsonic ($M_{r,1} = 0.97$ and $M_{r,2} = 0.93$ at the inlet). However, as the fundamental mode evolves downstream, $M_{r,2}$ becomes supersonic and Mach wave radiation is also seen at that frequency. A rough estimate of the wavefront geometry in the lower stream of figure 3(*a*) gives a Mach angle of $\approx 60^\circ$, corresponding to the downstream value of $M_{r,2} = 1.15$ in figure 2(*a*).

On the other hand, the values of $M_{r,i}$ remain firmly subsonic for the entire domain for the M050M025 mixing layer, and the acoustic radiation mechanism is distinctly different. Rather than strongly emitting sound at a particular angle downstream, the majority of the sound in the subsonic mixing layer originates from a single point inside the shear layer. The inclusion of both the fundamental and the subharmonic frequency in the subsonic mixing layer leads to vortex roll up, and consequently, vortex pairing occurring near the apparent acoustic source origin. This correlation was noted previously by Ho & Huang (1982) and in the work of Colonius, Lele & Moin (1997). In addition, the location of vortex pairing is linked to the point of saturation for the subharmonic and fundamental modes. From figure 4(*b*), one can determine that the maximum modal energy, as determined by (A 2), for the subharmonic (E_1) and

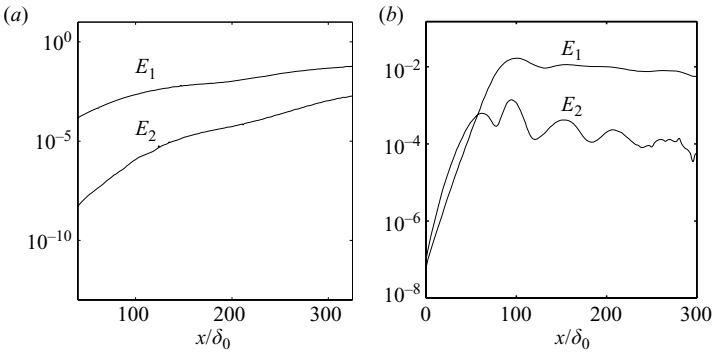

FIGURE 4. (*a*) Modal energy for the fundamental mode ($E_1(x)$) and first harmonic ($E_2(x)$) of the supersonic mixing layer M29M1. (*b*) The modal energy for the subharmonic ($E_1(x)$) and fundamental ($E_2(x)$) mode of the subsonic mixing layer M050M025.

the fundamental (E_2) also occurs near $x \approx 100$, and around this location the largest nonlinear interactions between the two modes can be expected to occur.

In contrast, the nonlinear interactions of simulation M29M1 alter the characteristics of the hydrodynamic near field to a lesser degree, but still influence the resulting sound field. The near-field vorticity in figure 3(*a*) shows a lack of vortex pairing due to the absence of the subharmonic frequency, and less well-defined vortex roll up compared to the subsonic M050M025 mixing layer. However, nonlinear interactions play a significant role in the excitation of the first harmonic, which can also radiate strongly to the far field. Unlike the fundamental mode, the first harmonic is not forced at high amplitudes at the inlet, but grows to an appreciable amplitude due to interactions with other modes (see figure 4*a*). The radiation patterns of the first harmonic are similar to the Mach wave radiation of the fundamental, as discussed in § 4.1.

Lastly, the direct calculations of the supersonic and subsonic mixing layers also illustrate differences in the behaviour of the pressure eigenfunction, depending on the phase speed of the instability wave relative to the free stream. In the subsonic M050M025 mixing layer, the phase speed of the instability wave is subsonic relative to both streams, leading to two distinct regions of behaviour. Close to the sheared region of the flow, the pressure eigenfunction exhibits purely exponential decay in the y-direction, which is the expected behaviour from classical instability wave theory (figure 5*b*). For $|y| > 15$, however, the pressure eigenfunction transitions to a slower algebraic decay, which would signal a shift to acoustic wave propagation. In the corresponding figure for the supersonic mixing layer (figure 5*a*), this transition in the pressure $\hat{P}_1(y)$ only occurs on the upper stream side, where $M_{r,1} = 0.855$ at the location $x = 275$. In the lower stream, where the relative phase speed $M_{r,2} = 1.04$ at the same location, the instability wave is directly coupled to acoustic disturbances propagating in the free stream and a very slow exponential decay persists, becoming visible as Mach wave radiation.

4. Linear and nonlinear stability calculations

The extent to which linear and nonlinear stability calculations can capture the flow and acoustic behaviours observed in § 3 is examined next using a series of PSE simulations. The results for the supersonic mixing layer are discussed first, followed by the computations for the two subsonic cases.

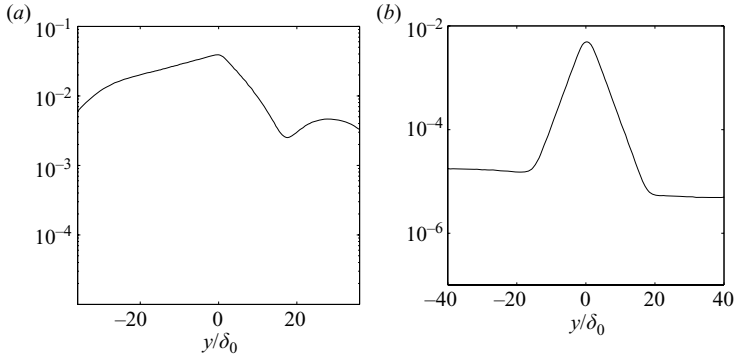

FIGURE 5. Pressure cross-sections $|\hat{P}_1(y)|$ for (*a*) M29M1 mixing layer at $x = 275$ and (*b*) M050M025 mixing layer at $x = 250$.

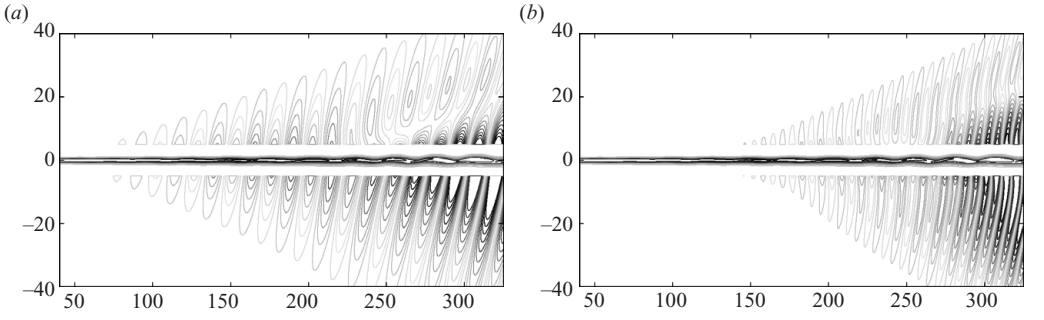

FIGURE 6. (*a*) Pressure field $\mathrm{Re}\{\hat{P}_1\}$ of the fundamental mode, as calculated by nonlinear PSE, plotted using same contours as figure 3(*a*). (*b*) Pressure field $\mathrm{Re}\{\hat{P}_2\}$ of the first harmonic, plotted using contours from -2.75×10^{-3} to 2.75×10^{-3} in steps of 2.75×10^{-4}.

4.1. *Supersonic mixing layer*

4.1.1. *Acoustic and near-field predictions*

The ability of nonlinear PSE to capture the acoustic and hydrodynamic behaviour of the supersonic mixing layer M29M15 is shown qualitatively in figure 6. Strong Mach wave radiation is encountered at both the fundamental and first harmonic frequencies, and matches the acoustic behaviour of the direct calculation shown in figure 3(*a*). The angle of the Mach wave radiation to the upstream axis matches the values determined from the results of § 3. At the fundamental frequency, the Mach angle in the lower stream agrees with the previously estimated 60°, and measurements of the Mach wave give a value of $M_{r,2} \approx 1.05$ for the first harmonic mode, which is in close agreement with the value obtained from the direct calculation.

Contours of the spanwise vorticity plotted in figure 7 show that large-scale features of the flow are well represented by the current instability wave model. The streamwise evolution of the instability waves responsible for creating vortical structures in the flow is illustrated in figure 8(*a*). The growth of the modal energy $E_1(x)$ at the fundamental frequency and $E_2(x)$ at the first harmonic closely follows the results from the direct calculations. Similarly, the behaviour of the acoustic pressure $\hat{P}_m$ in both the streamwise and cross-stream directions is consistent with the Mach wave radiation previously observed. In figure 8(*b*), we can see that the strength of the

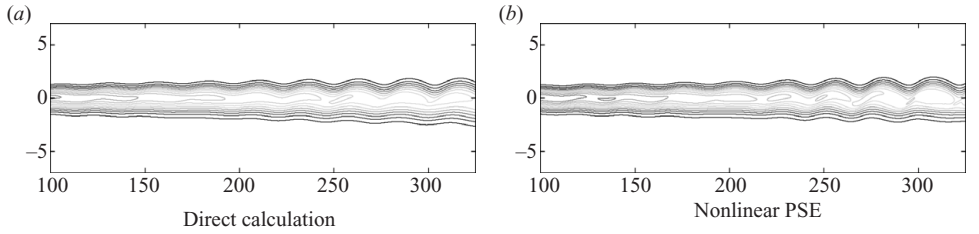

FIGURE 7. Near-field vorticity contours for the M29M1 mixing layer, computed by (*a*) direct calculation and (*b*) nonlinear PSE. Contours range from −1.5 to 1.5 in steps of 0.1.

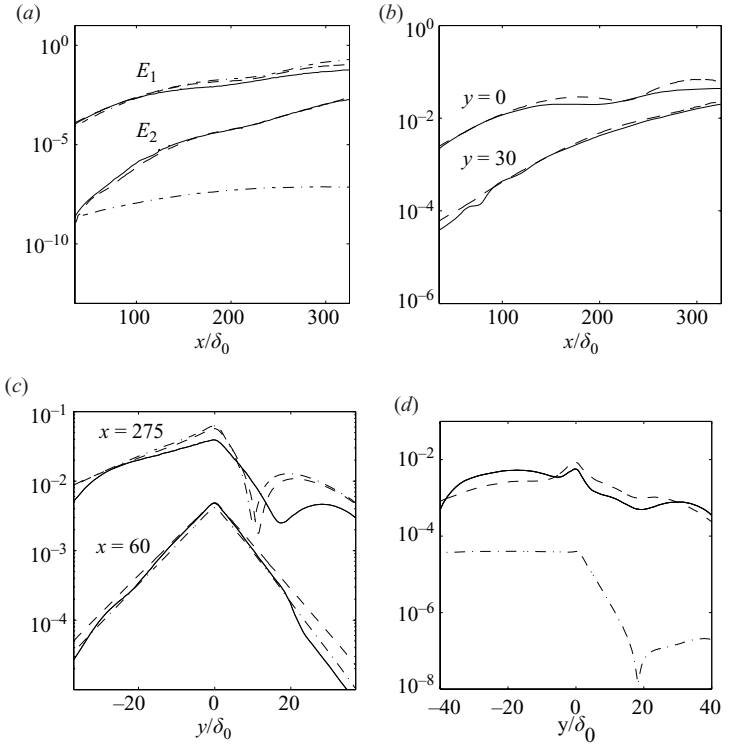

FIGURE 8. (*a*) Integrated modal energy $E_1(x)$ for the supersonic mixing layer M29M1. (*b*) streamwise pressure behaviour $|\hat{P}_1(x)|$ at $y = 0$ and $y = -30$. (*c*) The pressure $|\hat{P}_1(y)|$ at $x = 60$ and $x = 275$ at the fundamental frequency. (*d*) The pressure $|\hat{P}_2(y)|$ at $x = 290$ at the first harmonic. Direct calculation: solid line (——), nonlinear PSE: dashed line (— —), linear PSE: dash-dot line (— · —).

radiated pressure $\hat{P}_1(x, y = -30)$ is directly linked to the growth of the instability wave itself, and the difference in downstream eigenfunction behaviour, depending on whether $M_{r,i}$ is supersonic or subsonic (figure 8*c*).

4.1.2. *Nonlinear effects*

The effects of nonlinearity can be easily shown by comparing the nonlinear calculations with results from linear PSE and direct calculations. At the fundamental frequency, the evolution of the instability wave is well captured by the linear calculation (figure 8*a*), and the radiated Mach waves show good agreement with

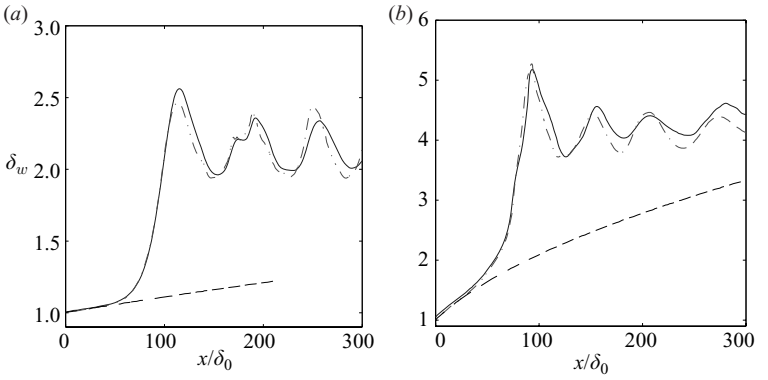

FIGURE 9. Comparison of the mean vorticity thickness for (*a*) M25M15 and (*b*) M050M025 subsonic mixing layer. Direct calculation: solid line (——), nonlinear PSE: dashed-dot line (– · –), linear PSE: dashed line (— —).

previous calculations. On the other hand, linear predictions for the development of the first harmonic diverges with results from both nonlinear PSE and direct calculations. The initial amplitude of the first harmonic in the linear PSE simulation is identical to the nonlinear case, but the growth rates remain constantly lower. As a consequence, the far-field acoustic radiation is severely underestimated at this frequency (figure 8*d*). This suggests that in order to accurately account for the Mach wave emission at all of the radiating frequencies, nonlinear interactions between instability modes must be included.

4.2. *Nonlinear effects in subsonic calculations*

The presence of nonlinear effects become more visible in the two subsonic mixing layers M25M15 and M050M025. As instability waves cause vortex roll up and pairing to occur in the subsonic mixing layers, nonlinear mechanisms such as the mean flow correction and the transfer of energy between modes drastically alter the downstream evolution of the overall mixing layer. The precise influence of these nonlinear effects can be determined using a series of three PSE computations of the subsonic mixing layers.

In the first series, a purely linear stability theory (linear PSE) is used to calculate the behaviour of the instability waves *without* the presence of a mean flow correction and *excludes* the possibility of nonlinear interactions between modes. The second set of calculations uses a partially linear theory, where linear PSE is used *with* a previously computed mean flow correction but still excluding nonlinear interactions. The third set of calculations is fully nonlinear, using nonlinear PSE with the mean flow correction and including all interactions between modes.

For both subsonic mixing layers, the correction to the mean flow was quite sizable, and was seen to have a large effect on the evolution, and hence, acoustic behaviour of the instability modes. At its peak location near the point of saturation, the corrected mean flow vorticity thickness was two to three times the uncorrected value (figure 9). Nevertheless, the mean flow correction procedure in the full nonlinear PSE calculations accurately predicted the growth of the mean flow.

The sudden expansion of the mean flow due to vortex pairing led to significant changes in instability wave growth. In the linear and nonlinear cases where the mean flow correction was included, the location of maximum vorticity thickness also corresponded to the saturation locations of the first two instability modes (figure 10).

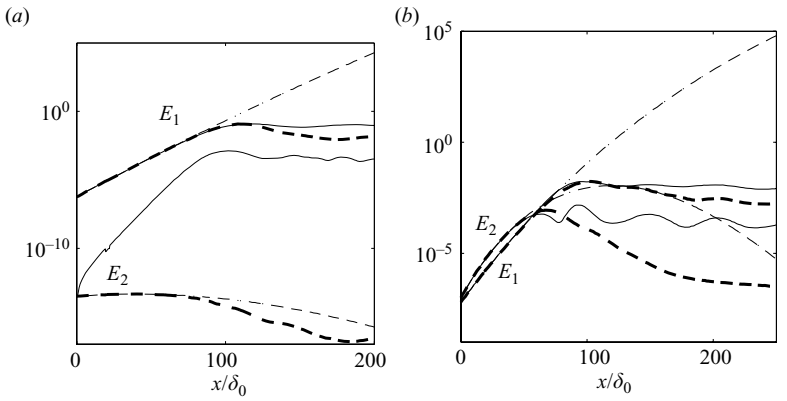

FIGURE 10. Comparison of energies for the linear and nonlinear PSE simulations. (*a*) M25M15, (*b*) M050M025 subsonic mixing layer. Fully nonlinear PSE: solid line (——), fully linear PSE: thin dash-dot line (– · –), linear PSE with mean flow correction: thick dashed line (– – –).

In the case of the purely linear PSE simulations, the absence of any mean flow correction resulted in continued exponential growth for the first two modes. While all calculations yielded similar growth rates in the linear regions of the flow, using a purely linear theory without compensating for the mean flow would lead to unreasonably large amplitudes for these modes. These observations are consistent with the findings of Hultgren (1992).

Nonlinear interactions between modes also played a significant role in determining the proper final amplitudes for instability modes. Using a linear PSE approach with mean flow correction captured the eventual saturation of the fundamental mode (E_2) of mixing layer M050M025, but a fully nonlinear theory is required to predict the correct saturation amplitude. The inclusion of nonlinear interactions is also required to capture the growth of higher harmonics. The fully or partly linear PSE calculations predict that the first harmonic mode (E_2) of M25M15 remains relatively neutral, and stays at a relatively small amplitude before eventually decaying downstream (figure 10*a*). However, under the fully nonlinear theory, the first harmonic is correctly shown to be initially unstable, and eventually reach a point of saturation.

The physical differences in the flow between the linear and nonlinear PSE calculations are illustrated in figures 11 and 12. When compared to the equivalent vorticity contours from the direct calculations, we can conclude that the linear PSE calculations fail to completely capture the vortex roll up and pairing mechanisms. In the uncorrected linear PSE simulations, the perturbations in the fundamental mode lead to alternating patterns of vorticity, but the roll up phenomena is not present. The unbounded growth of the mode also causes increasingly high concentrations of vorticity which eventually exceed the contours of the plot. The inclusion of the corrected mean flow helps to alleviate this problem, but the vortex roll up pattern is still seen to be incomplete. In figure 12, the mean flow corrected linear PSE simulation for M050M025 eventually results in discrete vortices, but the pairing process near $x = 100$ is still very different from the phenomena shown by the corresponding nonlinear PSE or direct calculation plots.

Comparisons of the fully nonlinear PSE simulations with the equivalent direct calculations show the importance of including the mean flow correction and modal interactions. Once both effects are accounted for, the large-scale vortical structures

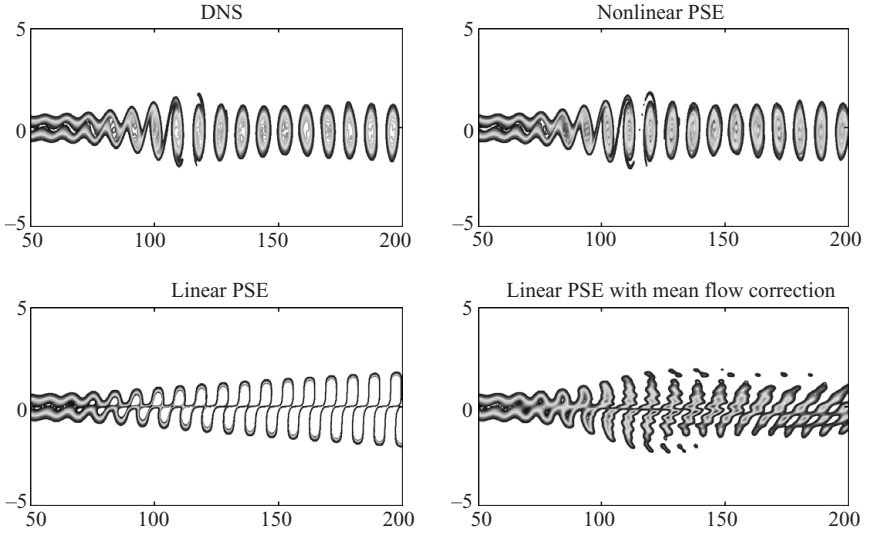

FIGURE 11. Spanwise vorticity contours ω_z for the subsonic mixing layer M25M15, as computed by direct calculation (upper left), nonlinear PSE (upper right), linear PSE (lower left) and linear PSE with corrected mean flow (lower right). Contour levels range from −1.0 to −0.3 in steps of 0.025.

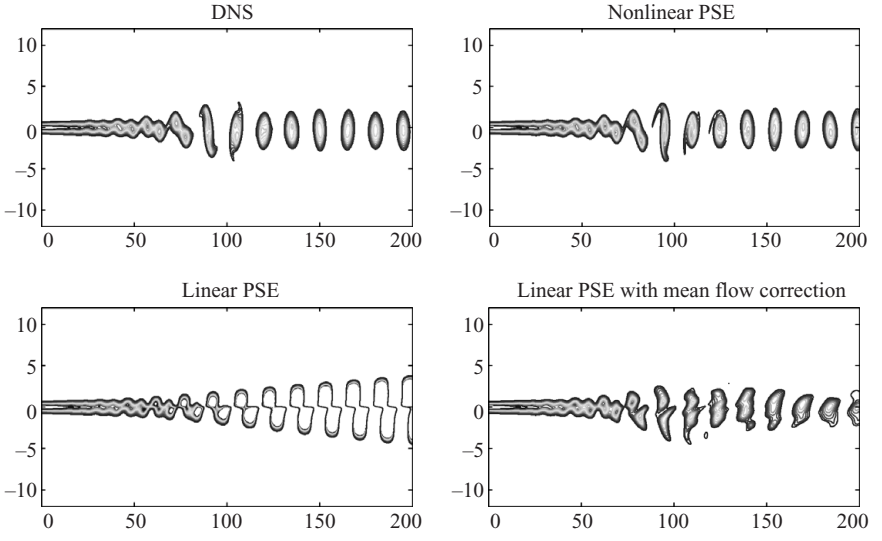

FIGURE 12. Spanwise vorticity contours ω_z for the subsonic mixing layer M050M025, as computed by direct calculation (upper left), nonlinear PSE (upper right), linear PSE (lower left) and linear PSE with corrected mean flow (lower right). Contour levels range from −0.20 to −0.05 in steps of 0.01.

computed from instability theory closely match those from direct computations. These results are in good agreement with the findings of Day *et al.* (2001), who also compared linear and nonlinear PSE simulations of reacting mixing layers. The implications of these nonlinear effects for sound radiation are stressed in the present paper.

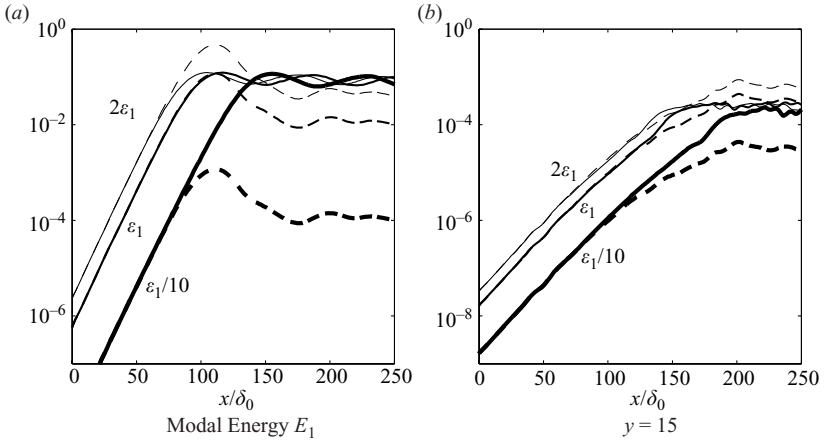

FIGURE 13. (*a*) Integrated modal kinetic energy E_1 for the fundamental mode with initial amplitudes $2\epsilon_1$, ϵ_1 (thicker lines) and $\epsilon_1/10$ (thickest lines). (*b*) Pressure magnitudes $|\hat{P}_1(x)|$ at $y/\delta_0 = 15$ of the fundamental mode. Nonlinear PSE: solid lines (——). Linear PSE: dashed lines (— —).

4.3. *Initial amplitudes and saturation location*

From the results shown in § 4.2, one could surmise that if the correct mean flow were obtained, linear theory would be sufficient in predicting the evolution for the most unstable instability waves. However, the initial amplitudes of the instability modes provided at the inlet can also play a large role in determining the downstream dynamics of the mode, and ultimately the emitted sound from the mixing layer. In the following section, we show the necessity of using both the corrected mean flow and the corresponding initial mode amplitudes in order to obtain correct predictions from linear theory.

For the subsonic M25M15 mixing layer, three pairs of linear and nonlinear PSE simulations were computed, with each pair of simulations using a different initial amplitude ($2\epsilon_1$, ϵ_1 or $\epsilon_1/10$) for the fundamental mode. In the nonlinear PSE simulations, the higher harmonics were fully coupled and the mean flow correction appropriate to the set initial amplitude was accounted for. In all of the complementary linear PSE simulations, only the corrected mean flow corresponding to the ϵ_1 case was used, but the simulations did not include any coupling to the instability modes. Hence, for the $2\epsilon_1$ and $\epsilon_1/10$ linear PSE simulations, there exists a mismatch between the corrected mean flow and the corresponding initial amplitude of the instability wave.

Comparisons of the modal kinetic energy growths are shown in figure 13(*a*). As expected, the fundamental mode in the linear PSE simulations behave identically, except for a scaling factor determined from the initial amplitude. Following an initial exponential growth region, all of the linear PSE modes saturate at the same downstream position, and the final amplitudes vary according to the scaling factor. On the other hand, the fundamental modes in the nonlinear PSE simulations saturate at different downstream positions depending on their initial amplitude, while the saturation amplitudes remain approximately constant. Similar behaviour for the pressure amplitudes away from the centreline is shown in figure 13(*b*). The far-field pressures from the nonlinear PSE simulations all converge to approximately the same

amplitude downstream, while the pressure amplitudes from the linear PSE simulations depend on their initial amplitudes.

From these comparisons, we can conclude that for a given instability mode (close to the most unstable mode), the saturation amplitudes and saturation location are correctly predicted by linear theory only if both the correct mean flow and corresponding initial amplitudes are provided. Because some of this information cannot be found through linear theory alone, it appears that some elements of nonlinearity must be incorporated to obtain an accurate picture of the most unstable instability wave evolution. As noted earlier, nonlinear effects are much stronger for other instability modes which grow via mode–mode interactions.

5. Subsonic mixing layers – acoustic radiation

The previous section demonstrated the influence of nonlinear interactions and mean flow corrections in predicting the evolution of instability waves inside the shear layer. In this section, we now consider the far-field behaviour for the fully nonlinear subsonic simulations. Of particular interest is the transition of the instability wave from 'hydrodynamic' behaviour in the near-field region to 'acoustic' behaviour in the far field. Results from the nonlinear PSE simulation of M050M025 are shown along with the complementary results from the direct calculations mentioned in § 3. Because the phase speed of the fundamental and subharmonic mode of M050M025 are subsonic relative to both streams of the mixing layer, the instability waves are not directly coupled to the far field, and the sound generation mechanism in this case is due to vortex pairing.

The first comparisons shown in figure 14(*a*) depict the streamwise evolution of the pressure $\hat{P}_1$ at the subharmonic frequency at two vertical locations: inside the shear regions of the flow (at $y = 0$) and in the far field ($y = 30$). In the near-field region of the flow the pressure fluctuations grow exponentially during the initial linear instability phase, before eventually saturating near the vortex pairing location. Not surprisingly, the growth rate and the saturation amplitudes for $\hat{P}_1(x, y = 0)$ along the centreline are well predicted by the nonlinear PSE computation. However, in the acoustic field, the predictions from nonlinear PSE begin to diverge from the direct calculation. At $y = 30$, the PSE calculations generally underpredict the pressure radiated to the far field by an order of magnitude or greater, except near the vortex pairing location, where the pressures are comparable. In contrast to the radiation patterns of the supersonic mixing layer, sound is radiated in both the downstream and upstream directions of the vortex pairing. From this near-field data it is not clear whether the acoustic radiation is 'superdirective' or a simpler composition of multipole fields.

This behaviour is further explored by considering the cross-sections of the pressure in the y-domain at different streamwise locations. In figure 14(*b*), the subharmonic pressure $\hat{P}_1(x = 50, y)$ is considered at a point upstream of the vortex pairing location. The direct calculation and nonlinear PSE calculation both agree in the near field region ($|y| \leqslant 20$), but the pressure calculated by PSE decays to much lower levels than its directly computed counterpart. The directly calculated pressure shifts to the slower algebraic decay at an earlier point than PSE, leading to a larger amplitude predictions in the far field.

Near the vortex pairing location the far field behaviour of the pressure is more comparable between the two methods of calculation. At the streamwise location of $x = 125.0$ (figure 14*c*), both calculation methods predict a similar transition point to the slower algebraic decay of the pressure eigenfunction. Near this location the

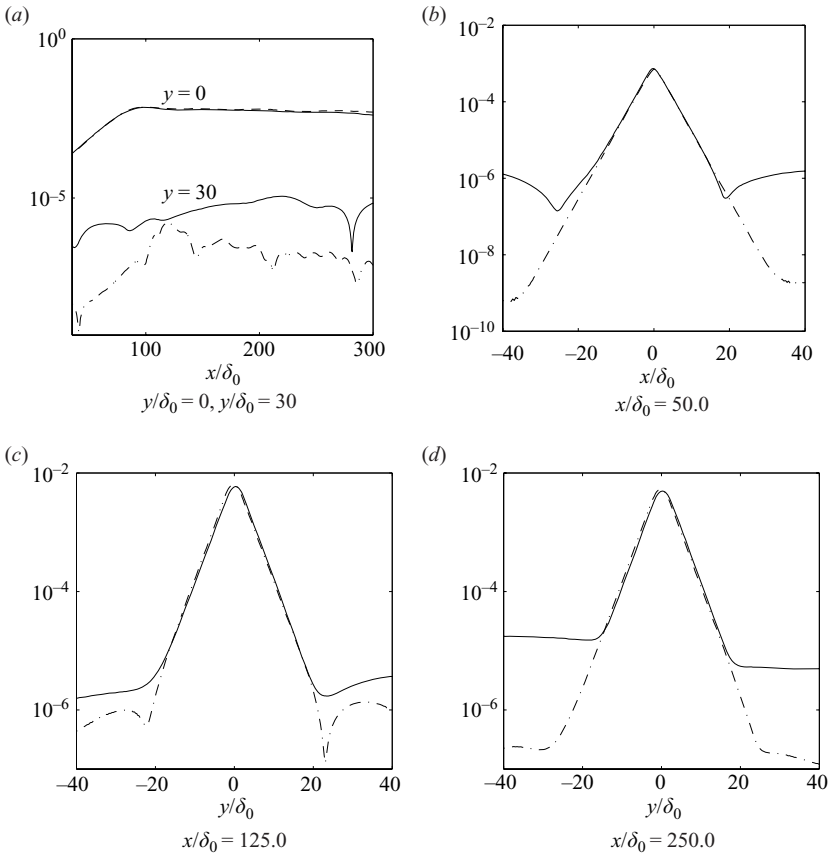

FIGURE 14. The streamwise pressure $|\hat{P}_1(x)|$ for the subsonic M050M025 mixing layer (*a*) along $y = 0$ and $y = 30$. Also shown are the cross-stream pressure $|\hat{P}_1(y)|$ at downstream positions (*b*) $x = 50$ (*c*) $x = 125$ (*d*) $x = 250$. Direct calculation: solid lines (——). NPSE: dashed-dot lines (– · –).

far-field pressures calculated by the PSE simulation are generally on the same order of magnitude. For the M050M025 mixing layer this region of agreement is limited to a small region around the vortex pairing location, near $120 \leqslant x \leqslant 130$.

Further downstream of the vortex pairing location the PSE predictions and direct calculations of the far field again diverge. At position $x = 250.0$ (figure 14*d*), the pressure calculated by nonlinear PSE is approximately two orders of magnitude smaller than the direct calculations. Inside the near-field region, however, the PSE method correctly predicts the hydrodynamic behaviour for both the subsonic shear layers.

6. Acoustic analogy

In previous sections, we noted that nonlinear instability wave theories could correctly predict the near-field hydrodynamic behaviour of subsonic mixing layers, but underpredicted the far-field acoustic radiation emanating from the vortex roll up and pairing triggered by the instability. In this section we show it is possible to combine the instability wave approach with an acoustic analogy, and properly capture the acoustic

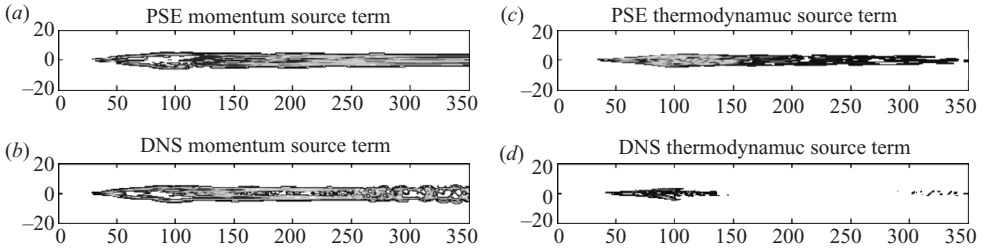

FIGURE 15. Plot of the source term magnitudes $|\hat{\Gamma}_m|$and $|\hat{\Gamma}_t|$ for the subsonic mixing layer M050M025. Contours for (*a*) and (*b*) range from 10^{-6} to 10^{-5} in steps of 10^{-6}. Contours for (*c*) and (*d*) range from 10^{-7} to 10^{-6} in steps of 10^{-6}.

wave propagation. We demonstrate both the accuracy of the source terms computed using nonlinear PSE information and the predictions obtained from applying Lilley's acoustic analogy. Lastly, we discuss the importance of using nonlinear theory in computing the source terms versus using a purely linear theory.

6.1. *Source terms*

We first consider the overall structure of the source terms computed by the nonlinear PSE and direct computations for the M050M025 mixing layer. As described by (A 13) and (A 14), the source term at the subharmonic frequency $\hat{\Gamma}_1(x, y)$ can be divided into momentum ($\hat{\Gamma}_m$) and thermodynamic ($\hat{\Gamma}_t$) components in order to assess their relative contributions to the predicted far-field sound. The linearized version of the inhomogeneous Lilley–Goldstein equation also requires a parallel mean flow $\bar{\boldsymbol{\phi}}(y)$, which we take near the point of subharmonic saturation, at $x = 100$, for the M050M025 mixing layer. The sensitivity of the acoustic predictions to the choice of the mean flow location is discussed in § 6.4. Also, in the computation of the nonlinear PSE, the inlet amplitudes ϵ_1 were not altered and consistent with the mean flow used in the Lilley–Goldstein equation.

A qualitative assessment of the source terms $\hat{\Gamma}_m$ and $\hat{\Gamma}_t$ is provided by the contour plots in figure 15. When the results from the nonlinear PSE calculations are compared against their directly computed counterparts, we can see that the magnitude and extent of the source terms have been relatively well predicted. The peak source terms occur near the vortex pairing location and are relatively limited in the transverse direction. The thermodynamic source terms in figure 15(*c*, *d*) are also an order of magnitude smaller than the momentum source terms, as would be expected for an isothermal mixing layer.

Cross-sections of the source terms for the isothermal subsonic shear layer in figure 16 provide a more quantitative examination of the source term structure. In figure 16(*a*), the transverse structure of the momentum and thermodynamic source terms is shown at the location of vortex pairing ($x = 100$) and the compact nature of the source terms in the y-direction is visible. Both nonlinear PSE and direct calculations predict that the source terms decay exponentially rapidly outside the range $-10 \leqslant y \leqslant 10$ and are essentially negligible in the free stream. From figure 16(*b*), the streamwise structure of the momentum source term $\hat{\Gamma}_m(x, y = 0)$ involves an initial development region from about $0 \leqslant x \leqslant 60$, also peaks near the vortex pairing location. Downstream of the vortex pairing location the source terms decay by approximately an order of magnitude by $x = 200$. As noted previously, the thermodynamic source terms for the M050M025 mixing layer are small compared to the momentum source terms. Although the nonlinear PSE version predicts a slightly

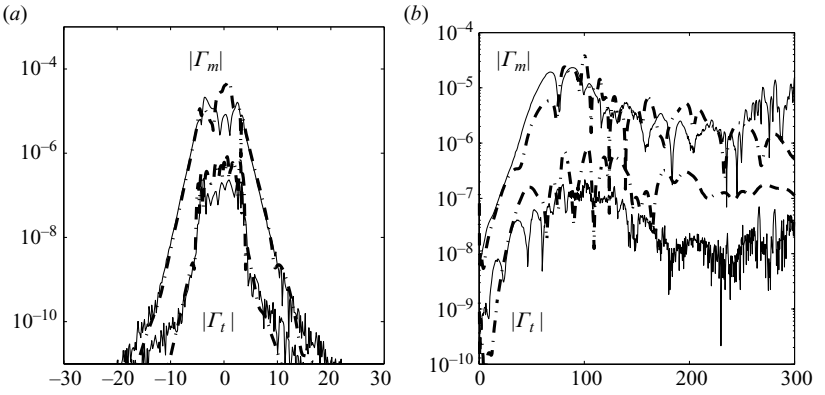

FIGURE 16. Source terms for the isothermal subsonic shear layer. (*a*) Cross-section of source terms $|\hat{\Gamma}_m(y)|$ and $|\hat{\Gamma}_t(y)|$ at $x = 100$. (*b*) Cross-section of source terms $|\hat{\Gamma}_m(x)|$ and $|\hat{\Gamma}_t(x)|$ at the centreline $y = 0$. Direct calculation: solid lines (——). NPSE: thick dashed-dot lines (– · –).

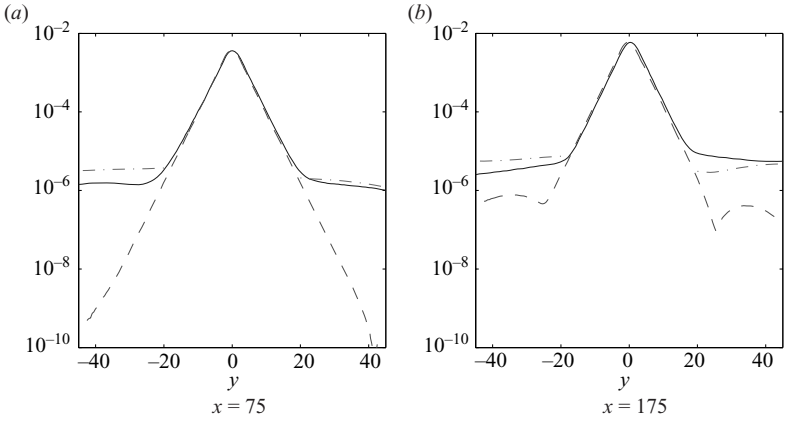

FIGURE 17. Far-field acoustic predictions from DNS, PSE and hybrid PSE-acoustic analogy methods for the isothermal subsonic shear layer. (*a*) $|\hat{P}_1(y)|$ at $x = 75$ and (*b*) $|\hat{P}_1(y)|$ at $x = 175$. Direct calculation: solid line (——), PSE: dashed line (— —), Lilley's equation: dashed-dot line (– · –).

higher peak for $\hat{\Gamma}_t(x, y = 0)$ than the direct computation, it is still negligible compared to the momentum source term.

6.2. *Lilley's far-field predictions*

Given the source terms calculated in § 6.1, we now make use of the acoustic analogy to recover the acoustic field that was missing from the nonlinear PSE solution. By employing (A 16) to calculate the far field pressures, we can compare the new predictions to values previously obtained from the nonlinear PSE and direct calculations.

In figure 17 we re-examine the near-field and far-field pressure behaviours of the subsonic M050M025 mixing layer. Upstream of the vortex pairing location at $x = 75$, the calculations from Lilley's equation correctly predict the far-field behaviour in the upper and lower free stream, while the pressure eigenfunction in the PSE

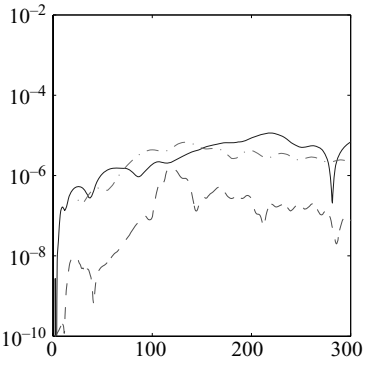

FIGURE 18. Far-field acoustic predictions, $|\hat{P}_1(x)|$ at $y = 30$, from DNS, PSE and hybrid PSE-acoustic analogy methods for the isothermal subsonic shear layer. Direct calculation: solid line (——), PSE: dashed line (— —), Lilley's equation: dashed-dot line (— · —).

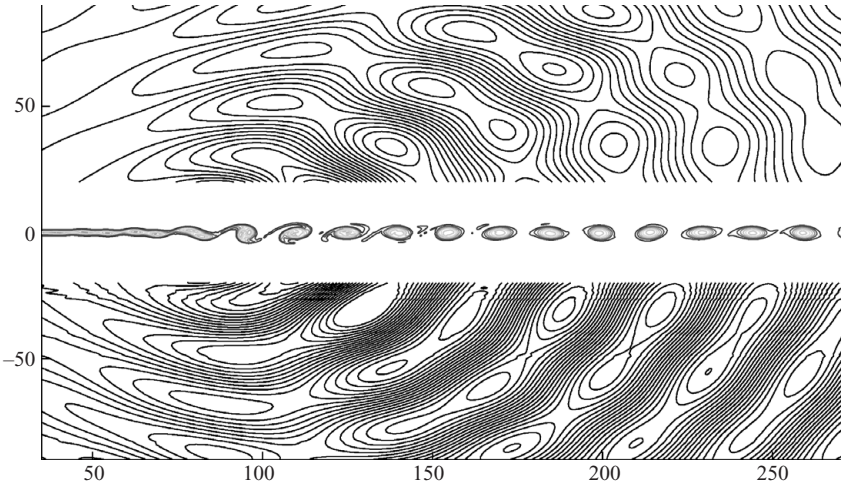

FIGURE 19. Far-field acoustic predictions, $\mathrm{Re}\{\hat{P}_1(x, y)\}$ using Lilley's acoustic analogy on the subsonic M050M025 mixing layer. Pressure contours are the same as in figure 3(*b*).

method continues to decay exponentially. Downstream of the vortex pairing location, at $x = 175$, the predictions from Lilley's acoustic analogy also correctly predict the amplitude of sound radiated away, while the PSE method alone underestimates the pressure by approximately an order of magnitude.

The streamwise behaviour of the far-field pressure is also improved using predictions from the combined nonlinear PSE-acoustic analogy approach. Whereas much of the upstream and downstream sound is absent from nonlinear PSE calculations, the pressure amplitudes $|\hat{P}(x, y = 30)|$ given by the acoustic analogy predictions are comparable to the directly calculated pressures (figure 18). Finally, the radiation patterns shown in figure 19 illustrate the acoustic field resulting from vortex sound generation, and agrees qualitatively with figure 3(*b*) from the directly computed mixing layer.

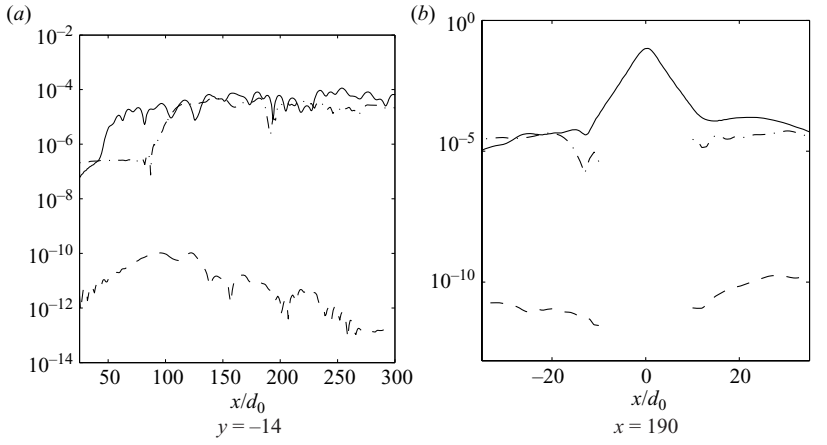

FIGURE 20. Comparisons of the pressure $|\hat{P}_1(x, y)|$ for the subsonic mixing layer M25M15, comparing results from the direct calculations (solid line, ——), Lilley's acoustic analogy with nonlinear source terms (dash-dot line, – · –) and Lilley's acoustic analogy with linear source terms (dashed line, — —).

6.3. *Linear versus nonlinear source terms*

In the next example of the combined PSE-acoustic analogy approach, we consider acoustic predictions for the subsonic M25M15 mixing layer and compare the effects of source terms calculated with and without nonlinearity. Two series of calculations were carried out, one using data from the nonlinear PSE, and the other using linear PSE.

In the first series, *nonlinear* PSE was used to calculate the source terms for the Lilley–Goldstein equation, and the predictions were compared against the direct calculations described in § 3. The comparisons for the pressure $\hat{P}_1$ at the fundamental frequency, shown in figure 20, resemble the predictions for the M050M025 subsonic mixing layer from § 6. The results from Lilley's acoustic analogy generally capture the levels of acoustic radiation in the far field, although the predictions for the lower stream are generally more accurate than in the upper stream. In the initial region ($0 < x < 114$), Lilley's predictions fail to capture sound emitted during the roll up and exponential development phase of the instability wave. The inaccuracy in this region may stem from the parallel flow assumptions used in the creation of the simplified source terms, since the actual mean flow is not strictly parallel near the vortex roll up and pairing locations. Hence, the associated Green's functions for the Lilley–Goldstein equation may be inadequate in capturing the upstream sound.

In the second series of calculations, Lilley's source terms were calculated from a *linear* PSE simulation with the corrected mean flow and excluding any modal nonlinear interactions. Additionally, the initial inlet amplitude ϵ_1 for the linear PSE and Lilley–Goldstein calculations were identical to the nonlinear PSE from the first series of calculations. The results obtained from these computations were again compared to the direct calculations and the nonlinear calculations discussed above. From figures 20(a) and 20(b), we can immediately observe that using linearly calculated source terms in the acoustic analogy produces little far-field noise. This can be explained, as in Sandham, Salgado & Agarwal (2008), by considering the quadratic nature of the Lilley source terms in (A 11b). A simple expansion of the source term at the fundamental frequency involves terms from both the fundamental $\hat{\boldsymbol{\phi}}_1$ and the

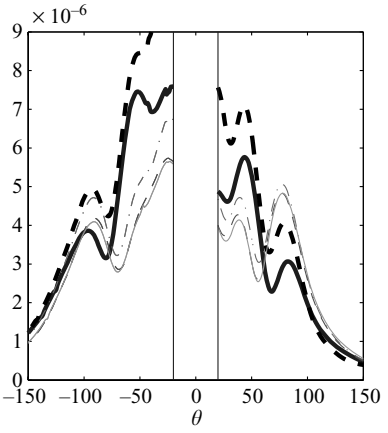

FIGURE 21. Sensitivity of Lilley's acoustic analogy predictions $|\hat{P}_1(\theta)|$ to mean flow profiles for M050M025 mixing layer. Mean flow profiles $\overline{\boldsymbol{\phi}}(y)$ chosen at the locations $x = 50$ (thick dashed line, – –), $x = 100$ (thick solid, ——), $x = 125$ (dash-dot – · –), $x = 150$, (thin dashed, — —), $x = 200$ (thin solid, ——).

first harmonic $\hat{\boldsymbol{\phi}}_2$. However, because the linear PSE calculations failed to properly excite the first harmonic (§4), the resulting source term at the fundamental is also inaccurate. Not surprisingly, when the source terms from linear PSE are examined in this particular case, we find that their typical amplitudes are several orders of magnitude below those computed from nonlinear PSE.

Taking these findings into consideration, we can make the following observations regarding the aeroacoustic behaviour of mixing layers. For instability waves with supersonic phase speed relative to one of the free streams, they are associated with a direct Mach wave radiation. This Mach wave radiation can be predicted using a linear stability wave theory, but only after appropriate accounting of the nonlinear effects. The instability wave growth rate and its saturation need to be accurately captured. However, for instability waves with a subsonic phase speed relative to the free stream, the sound radiation is due to a different physical mechanism – vortex pairing noise. Accurate predictions of the far-field sound in this case heavily depend on using the correct mean flow and accounting for nonlinear modal interactions. In addition, although nonlinear stability wave theory can capture the growth of the instability wave, it must be supplemented with an additional method such as an acoustic analogy to capture the acoustic radiation.

6.4. *Sensitivity to mean flow location*

As mentioned in §6.1, a preliminary study regarding the sensitivity of the acoustic field was conducted to determine the most appropriate choice of the mean flow profile $\overline{\boldsymbol{\phi}}(y)$ to use in Lilley's acoustic analogy. Our results indicated that the choice of the mean flow profile location can affect the directivity of Lilley's acoustic analogy predictions. This is shown in figure 21, where the pressure predictions $|\hat{P}_1(\theta)|$ are plotted for mean flows selected at various locations, using data sampled at a distance $R = 50$ away from the apparent source location, and where the angle θ is chosen to be 0° pointing in the downstream direction. From these results we can make two general observations.

First, for mean flow profiles located downstream of the instability wave and source term peak location, e.g. the profiles taken at $x = 125$, 150 and 200 in figure 21, the

directivity of acoustic radiation shifts towards higher angles. For these profiles the higher angle lobe at $\sim 75^\circ$ dominates over the lower angle lobe at 40°–45°, and radiation towards lower angles is suppressed. This contradicts earlier evidence from the direct calculations and previous studies of mixing layer aeroacoustics (Colonius *et al.* 1997), which have suggested that the peak acoustic radiation from vortex pairing should occur at angles less than 60°.

Secondly, for mean flow profiles located upstream of the sound source peak, the acoustic radiation peak at lower angles is recovered. However, using profiles located too close to the inlet or upstream of the vortex roll up location generally caused over-estimations of the far-field pressure, as in the case of the profile selected from $x = 50$.

Given these observations, the choice of the mean flow profile near the saturation location and sound source peak at $x = 100$ seems to avoid problems associated with the directivity and amplitude of the acoustic predictions, and this profile was used in all computations in §§6.1–6.3. However, from our preliminary investigations, the need for a comprehensive study on the sensitivity of Lilley's acoustic analogy to the mean flow profile is apparent. By using the non-parallel acoustic analogy formulation from Goldstein (2003), or the adjoint Green's function approach of Tam & Auriault (1998), better insight may be gained into the refraction of sound from a spreading mean flow.

Lastly, we also provide some comments regarding the effects of three dimensionality on the dynamics and aeroacoustics of the mixing layers discussed in this work. Although oblique modes were not considered as a part of this work, some previous studies have provided hints as to how three dimensionality may affect our current results. For supersonic mixing layers, the higher growth rate of oblique modes (Jackson & Grosch 1989) should lead to stronger acoustic radiation, but the mechanism of sound generation (Mach wave radiation) is expected to remain the same as in the two-dimensional case. For the subsonic case, the work of Rogers & Moser (1992) in incompressible mixing layers highlighted the collapse of rib vortices and the distortion of the vortex core in the formation of kinks along the rollers. The nonlinear mechanisms involved in these processes may also serve to generate or modify sound sources, similar to the role of the nonlinear vortex pairing process in the creation of sound sources in the two-dimensional case.

7. Conclusions

In this paper, we examined the linear and nonlinear behaviour of instability waves in two-dimensional mixing layers, and highlighted the influence of nonlinearity to the dynamics and aeroacoustics of the shear layers. The effects of nonlinear interactions, mean flow correction and inlet amplitude conditions were examined using a combination of direct calculation, linear and nonlinear stability methods. Both supersonic and subsonic compressible mixing layers were considered.

From the results of our computations, several general observations appeared regarding the linear and nonlinear processes in mixing layers can be made. First, nonlinear interactions are largely responsible for the excitation and development of the higher harmonic instability waves. Even in cases where the primary instability mode behaves linearly (over a specific region of the flow), nonlinear coupling will trigger the growth of higher harmonics which can contribute to the acoustic radiation that is missing from the purely linear analysis. Secondly, the mean flow correction generated by finite amplitude instability modes was observed to be critical

in determining the appropriate saturation levels of instability modes. Using a linear theory without any mean flow modification resulted in non-physical instability wave amplitudes downstream, and a fully nonlinear treatment with mean flow correction was required to predict the development of instability waves past the saturation point. In addition, both the nonlinear interactions and mean flow correction were observed to be necessary in capturing the dynamics of large-scale vortical structures in the near field.

Similarly, the results of several computations illustrated the need for a fully nonlinear theory in order to predict the effects of the inlet conditions on the dynamics and acoustics of the mixing layer. While linear theory predicts a similar saturation location for all instability waves regardless of initial inlet amplitude, nonlinear effects were vital in determining position of the vortical structures, and consequently, the noise source locations. Based on these observations, the need to account for the interaction between the mean flow and the instability waves, and among the instability waves themselves, becomes apparent.

The effects of nonlinearity could also be seen in the aeroacoustic behaviour of the mixing layers as well. For supersonic mixing layers, where $M_{r,i} > 1$ in at least one fluid stream, the dominant mechanism of sound generation was Mach wave radiation. In these cases the far-field sound was directly coupled to the behaviour and growth of instability wave. Thus, the nonlinear interactions discussed above directly impacts the amplitude and structure of the Mach wave radiation. For subsonic mixing layers, where $M_{r,i} < 1$, the primary mechanism of sound generation is due to vortex pairing initiated by the interactions of the fundamental and subharmonic instability modes. In this instance, capturing the dynamics of the near-field vortical structures becomes critical and neither the nonlinear interactions nor the mean flow correction can be neglected.

Although nonlinear PSE provided an accurate description of the near-field hydrodynamic motions, its solution underestimated the acoustic pressure field for subsonically convected waves. However, by using source terms calculated from nonlinear PSE in the Lilley–Goldstein equation, the resulting far-field sound was found to be in good agreement with direct calculations. Lastly, this paper demonstrated the need to account for nonlinear interactions in computing the acoustic source terms. Using linear PSE to calculate the source terms in Lilley's acoustic analogy led to large underpredictions of the acoustic far field.

This work was sponsored by a National Defense Science and Engineering Graduate (NDSEG) Fellowship, and a National Science Foundation (NSF) Graduate Research Fellowship. Computational resources were provided in part by the Air Force Office of Science Research (AFOSR), contract number FA9550-04-1-0031.

Appendix A. Mathematical details

A.1. *Direct calculation*

Further details regarding the direct numerical simulation (DNS) of a single phase two-dimensional compressible mixing layer are presented in this section.

The variables in (2.1*a*)–(2.1*d*) have been non-dimensionalized using the initial vorticity thickness δ_0 and values from the upper stream, including the speed of sound a_1, density ρ_1, temperature T_1 and viscosity μ_1. The value for the ratio of specific heats in the upper stream $\gamma = c_{p,1}/c_{v,1}$ is taken to be 1.4. Finally, the non-dimensional

Reynolds number and Prandtl number are set to be $Re = \rho_1 a_1 \delta_0 / \mu_1$, $Pr = \mu_1 c_{p,1} / k_1$, respectively, where k_1 is the thermal conductivity of the fluid in the upper stream.

The solution to (2.1*a*)–(2.1*d*) were found through highly resolved numerical computations developed specifically for aeroacoustics applications. The basic numerical code was provided by Lui (2003), and used a sixth order compact finite difference scheme with spectral-like resolution (Lele 1992) in the transverse (y) and streamwise (x) directions. For time advancement, a two-step fourth-order Low Dissipation and Dispersion Runge–Kutta (LDDRK) scheme was employed. Sponge regions were placed in all outflow boundaries to suppress reflections and coordinate stretching in the y-direction allowed for an efficient allocation of grid points in the near- and far-field regions.

In order to obtain statistics in the frequency domain, data from the direct calculations were Fourier transformed in time, and instability wave energies were computed accordingly. The basic discrete transform

$$\hat{\boldsymbol{\phi}}'_m(x, y) = \frac{1}{N} \sum_{j=0}^{N-1} \boldsymbol{\phi}(x, y, t_j) \mathrm{e}^{\mathrm{i}\omega_m t_j} \tag{A 1}$$

was used where $\boldsymbol{\phi}$ is any fluid variable and N samples were gathered over a period $T = 2\pi/\omega_m$ at the frequency of interest. The values of $\hat{\boldsymbol{\phi}}'_m$ were computed by direct summation with either $N = 32$ or 64 samples obtained from the direct calculation.

One major statistic used in comparing the eigenmode behaviour between the direct calculation and PSE simulations is the integrated modal energy of the eigenmode. While the energy of the mode used in Day *et al.* (2001) involved only the kinetic energy components, the definition used here stems from the work of Chu (1965), and includes the energy due to temperature and density fluctuations.

$$E_m = \int_{-\infty}^{\infty} \left\{ \bar{\rho} \left(|\hat{u}'_m|^2 + |\hat{v}'_m|^2 \right) + \frac{\gamma - 1}{\gamma} \frac{|\hat{\rho}'_m|^2}{2\bar{\rho}} + \frac{\bar{\rho} \, |\hat{T}'_m|^2}{2\bar{T}} \right\} \mathrm{d}y \tag{A 2}$$

A.2. *PSE formulation*

A simpler more insightful model for the behaviour of the mixing layer can be utilized in cases where the inlet forcing is harmonic and the development of the shear layer is slow compared to the wavelength of the instability wave. Under these restrictions, the Navier–Stokes equations (2.1*a*)–(2.1*c*) can be reduced to a parabolized system governing the evolution of the instability waves and their nonlinear interactions. While the PSE approach has been largely standardized since its development by Bertolotti *et al.*, we provide a brief account of this method as it pertains to our work. Additional implementation details can be easily found in Malik & Chang (2000) and Day *et al.* (2001).

The model begins by separating the vector of flow variables $\boldsymbol{\phi} = [\rho \; u \; v \; T]^{\mathrm{T}}$ into mean $\bar{\boldsymbol{\phi}}$ and disturbance $\tilde{\boldsymbol{\phi}}$ components via the assumption $\boldsymbol{\phi} = \bar{\boldsymbol{\phi}} + \tilde{\boldsymbol{\phi}}$. The mean flow quantities $\bar{\boldsymbol{\phi}}$ are found through a similarity solution of the compressible boundary layer equations, as in Schlichting *et al.* (2004). The disturbance quantities $\tilde{\boldsymbol{\phi}}$ are assumed to be expressible as an expansion over eigenmodes $\hat{\boldsymbol{\phi}}_m$:

$$\tilde{\boldsymbol{\phi}}(x, y, t) = \sum_{m=-M}^{M} \hat{\boldsymbol{\phi}}_m(x, y) \mathscr{A}_m(x) \mathrm{e}^{-\mathrm{i}\omega_m t}, \tag{A 3}$$

where the amplitude portion $\mathscr{A}_m(x)$ is written as

$$\mathscr{A}_m(x) = \epsilon_m \exp\left\{ \mathrm{i} \int_0^x \alpha_m(x')\,\mathrm{d}x' \right\}. \tag{A 4}$$

In (A 3) and (A 4), an initial amplitude ϵ_m is provided for each eigenmode $\hat{\boldsymbol{\phi}}_m$, with an associated wavenumber α_m and temporal frequency ω_m. The temporal frequency of each mode is set to be an integer multiple of a base frequency ω, so that $\omega_m = m\omega$. In contrast to parallel linear stability theory, both $\hat{\boldsymbol{\phi}}_m$ and α_m are allowed to evolve downstream in x through a set of slowly varying assumptions. If the mean flow quantities $\bar{\boldsymbol{\phi}}$ evolve over a much longer length scale than the spatial wavelength of the instability wave, then the first derivatives of $\hat{\boldsymbol{\phi}}_m$ and α_m can be retained, and a parabolization of the governing equations is possible.

The slow rate of evolution in the mean flow usually translates into the assumptions

$$\frac{1}{Re}\frac{\partial \bar{\boldsymbol{\phi}}}{\partial x} \ll O(1) \quad \text{and} \quad \frac{\partial^2 \bar{\boldsymbol{\phi}}}{\partial x^2} \ll O(1), \tag{A 5}$$

and these terms can then be ignored in the derivation of the PSE. Similarly, the PSE restricts the downstream changes in the eigenfunction and growth rate by assuming that the terms

$$\frac{\partial^2 \hat{\boldsymbol{\phi}}_m}{\partial x^2} \ll O(1) \quad \text{and} \quad \frac{\partial^2 \alpha_m}{\partial x^2} \ll O(1), \tag{A 6}$$

and can be neglected as well. The final restriction on the disturbances admissible in PSE is that the instability waves are *convectively* unstable, and not *absolutely* unstable (Huerre & Monkewitz 1990). This ensures that for any given region, any oscillations will remain bounded in time.

Using (A 3) and the slowly varying assumptions (A 5) and (A 6) in the governing equations (2.1*a*)–(2.1*c*) yields a set of nonlinear disturbances equations (2.2) which form the basis of the nonlinear PSE method. The linear operator $\mathscr{L}_m$ can be broken down in terms of

$$\mathscr{L}_m = -\mathrm{i}\omega_m \boldsymbol{G} + \boldsymbol{A}\left(\mathrm{i}\alpha_m + \frac{\partial}{\partial x}\right) + \boldsymbol{B}\frac{\partial}{\partial y} + \boldsymbol{C}\frac{\partial^2}{\partial y^2} + \boldsymbol{D} + \frac{\partial \alpha_m}{\partial x}\boldsymbol{N}, \tag{A 7}$$

where the matrices $\boldsymbol{A}$, $\boldsymbol{B}$, $\boldsymbol{C}$, $\boldsymbol{D}$, $\boldsymbol{G}$ and $\boldsymbol{N}$ are functions of the mean flow variables $\bar{\boldsymbol{\phi}}$ only. The right-hand side of (2.2) contains the nonlinear forcing function $\mathscr{F}_m$ due to the higher order products of disturbances $\tilde{\boldsymbol{\phi}}$.

By removing all streamwise derivatives, and viscous terms, and setting $\bar{v} = 0$, the Rayleigh operator

$$\mathscr{L}_R\{\hat{\boldsymbol{\phi}}_m\} = \left\{-\mathrm{i}\omega_m \boldsymbol{G}' + \boldsymbol{A}'(\mathrm{i}\alpha_m) + \boldsymbol{B}'\tfrac{\partial}{\partial y} + \boldsymbol{C}'\tfrac{\partial^2}{\partial y^2} + \boldsymbol{D}'\right\}\hat{\boldsymbol{\phi}}_m \tag{A 8}$$

can be recovered from (A 7). Solutions to (A 8) are used as initial conditions to both the PSE calculations and the direct numerical calculations.

The linear PSE formulation is obtained from (2.2) by setting $\mathscr{F}_m = 0$. Because $\mathscr{L}_m$ contains only a single derivative in the x-direction, (2.2) can be efficiently solved through a streamwise marching procedure. A first-order backwards Euler method with variable step size was used to speed calculation and to avoid problems with numerical stability Andersson, Henningson & Hanifi (1998). In general, PSE computations required an order of magnitude fewer computational resources than the equivalent direct computations, usually about $O(10^2)$ versus $O(10^3)$ CPU-hours on an Intel Xeon

cluster. Further details regarding the form of (2.2), the slowly varying assumptions and the mean flow correction, are given in Appendix A 2.1 and Cheung (2007).

A.2.1. *Normalization conditions*

An additional constraint must be placed on (2.2) in order to make the system solvable. The need for this additional normalization constraint arises from the extra degree of freedom inherent in the representation (A 3) – streamwise variations of $\tilde{\boldsymbol{\phi}}(x, y)$ can be absorbed into either $\alpha(x)$ or $\hat{\boldsymbol{\phi}}(x, y)$. This ambiguity in x can be eliminated by placing an additional normalization constraint on either the eigenfunction, the eigenvalue or both. Many normalization conditions have been proposed that limit rapid changes in the eigenfunctions (Bertolotti *et al.* 1992). For this work, the usual integral norm is generalized to include all components of the eigenfunction $\hat{\boldsymbol{\phi}}$

$$\int_{-\infty}^{\infty} \left[W_1 \hat{\rho}_m^{\dagger} \frac{\partial \hat{\rho}_m}{\partial x} + W_2 \left(\hat{u}_m^{\dagger} \frac{\partial \hat{u}_m}{\partial x} + \hat{v}_m^{\dagger} \frac{\partial \hat{v}_m}{\partial x} \right) + W_3 \hat{T}_m^{\dagger} \frac{\partial \hat{T}_m}{\partial x} \right] \mathrm{d}y = 0, \tag{A 9}$$

where the weights W_1, W_2, W_3 correspond to different normalization conditions. For the kinetic energy based norm, we set the weights $W_1 = W_3 = 0$ and $W_2 = 1$. A second norm with weights $W_1 = (\gamma - 1)\bar{T}/\gamma\bar{\rho}$, $W_2 = \bar{\rho}$ and $W_3 = \bar{\rho}(\gamma - 1)/(\gamma^2 \bar{T}\bar{P})$ was also used to calculate the total disturbance energy (Chu 1965). In practice, the choice of weights had negligible impact on the overall results (Cheung 2007).

A.2.2. *Mean flow correction*

When the amplitude of the eigenfunctions in nonlinear PSE calculations reaches a finite size and modal interactions start to play an important role in the flow dynamics, the nonlinear terms will inevitably redistribute some amount of energy to the mode $\hat{\boldsymbol{\phi}}_0$ at zero frequency. This redistribution of energy indicates that the disturbances have grown to the extent that they are capable of modifying the mean flow, and a nonlinear correction to the mean flow is in order. This correction can be accommodated by adding components of the zero frequency mode to the original laminar mean flow components

$$\bar{\boldsymbol{\phi}}' = \bar{\boldsymbol{\phi}} + \hat{\boldsymbol{\phi}}_0(x, y)\mathscr{A}_0(x). \tag{A 10}$$

Although the zero-frequency mode is solved in a similar manner as all of the other finite-frequency modes, the mode is not present at the initial step of the PSE calculation. When the maximum of nonlinear forcing term $\hat{\boldsymbol{F}}_0$ exceeds a set threshold, the zero frequency mode is initialized by solving (2.2) with no $\partial/\partial x$ terms, and $\omega_0 = 0$, $\alpha_0 = 0$ initially. The growth of the mode is controlled by changes in $\alpha_{0,i}$, and the boundary conditions are identical to the conditions imposed on other modes. The influence and importance of the mean flow correction on shear layer flows is evident in some of the simulations, especially in cases where vortex pairing causes rapid changes to the thickness of the shear layer.

A.3. *Lilley's equation*

As mentioned previously, in some situations the instability wave model will fail to provide a complete description of the far-field acoustics for subsonic mixing layers. For these subsonic mixing layers, it becomes necessary to extend the formulation to include a model of the source terms and a method to propagate the solution to the far field. In the present case, we describe how the acoustic solution can be found through

an appropriate acoustic analogy using near-field source terms calculated from PSE and Lilley's wave equation.

Based on the work of Goldstein (2001), we express the acoustic analogy in terms of a parallel sheared flow $\bar{U}(x_2)$ with a source term composed of a velocity quadrupolar component and a fluctuating temperature dipole component

$$\bar{L}_0\pi = \frac{\mathrm{D}_0}{\mathrm{D}t}\frac{\partial f_i}{\partial x_i} - 2\frac{\partial \bar{U}}{\partial x_j}\frac{\partial f_j}{\partial x_1}, \tag{A 11a}$$

where

$$f_i = -\frac{\partial}{\partial x_j}(1+\pi)\tilde{u}_j\tilde{u}_i - \widetilde{c^2}\frac{\partial \pi}{\partial x_i} \tag{A 11b}$$

and $\widetilde{c^2} = (\gamma - 1)\tilde{T}$. The third-order linear operator is given by

$$\bar{L}_0 \equiv \frac{\mathrm{D}_0}{\mathrm{D}t}\left(\frac{\mathrm{D}_0^2}{\mathrm{D}t^2} - \frac{\partial}{\partial x_i}\overline{c^2}\frac{\partial}{\partial x_i}\right) + 2\frac{\partial \bar{U}}{\partial x_i}\frac{\partial}{\partial x_1}\overline{c^2}\frac{\partial}{\partial x_i}$$

where the material derivative is $\mathrm{D}_0/\mathrm{D}t = \partial/\partial t + \bar{U}\partial/\partial x_1$ and the pressure variable is

$$\pi = \left(\frac{P}{P_0}\right)^{1/\gamma} - 1. \tag{A 11c}$$

The source terms on the right-hand side of (A 11*a*) are evaluated using information from the PSE calculations. As shown in § A 3.1, the far-field pressure is solved by converting (A 11*a*) to a single ordinary differential equation through Fourier transforms in x and t.

In general, the solution to the parallel flow Lilley–Goldstein's equation will consist of a particular solution plus homogeneous solutions. Goldstein & Leib (2005) point out that these homogeneous contributions correspond to spatially growing instability waves which have the potential to grow unbounded far downstream in the flow. Their solution to this problem was to use a vector Green's function approach on a slightly non-parallel flow. The diverging non-parallel base flow would then ensure that the instability waves contributions grow and eventually decay. However, in this work, the mean flow $\bar{U}(x_2)$ is generally chosen at, or slightly after, the point of saturation of the eigenmode solution. After the point of saturation, the PSE solution for the instability waves were found to be either neutral or decaying, which would suggest that they would remain bounded downstream. On the other hand, if the base mean flow was set near the inlet position, where the fundamental and subharmonic instability waves were initially unstable, then the Goldstein & Leib concerns about the unbounded growth of the homogeneous solutions would apply.

A.3.1. *Solution to Lilley's equation*

The problem posed by the Lilley–Goldstein equation

$$\left[\frac{\mathrm{D}_0}{\mathrm{D}t}\left(\frac{\mathrm{D}_0^2}{\mathrm{D}t^2} - \frac{\partial}{\partial x_i}\overline{c^2}\frac{\partial}{\partial x_i}\right) + 2\frac{\partial \bar{U}}{\partial x_i}\frac{\partial}{\partial x_1}\overline{c^2}\frac{\partial}{\partial x_i}\right]\pi = \Gamma \tag{A 12}$$

in § A.3 can be converted into a single ordinary differential equation inthe transverse

direction y and solved numerically. Following Goldstein (2005), the source term Γ can be split into the momentum Γ_m and thermodynamic Γ_t components

$$\Gamma_m = \left[\frac{\mathrm{D}_0}{\mathrm{D}t}\frac{\partial}{\partial x_i} - 2\frac{\partial \bar{U}}{\partial x_i}\frac{\partial}{\partial x_1}\right]\left(-\frac{\partial}{\partial x_j}(1+\pi)\tilde{u}_j\tilde{u}_i\right), \tag{A 13}$$

$$\Gamma_t = \left[\frac{\mathrm{D}_0}{\mathrm{D}t}\frac{\partial}{\partial x_i} - 2\frac{\partial \bar{U}}{\partial x_i}\frac{\partial}{\partial x_1}\right]\left(-\widetilde{c^2}\frac{\partial \pi}{\partial x_i}\right). \tag{A 14}$$

For a given source term Γ, we can find the particular solution using a Fourier representation of π and Γ in the streamwise coordinate x and in time t

$$\pi(x, y, t) = \mathrm{e}^{-\mathrm{i}\omega t}\hat{\pi}(x, y) = \mathrm{e}^{-\mathrm{i}\omega t}\int \psi(k, y)\mathrm{e}^{\mathrm{i}kx}\,\mathrm{d}k. \tag{A 15}$$

Applying the transformation to (A 12), we obtain the inhomogeneous Rayleigh equation

$$\mathscr{L}\psi = \frac{\mathrm{i}\hat{\Gamma}(k, y)}{\omega^2(\bar{U}\kappa - 1)\overline{c^2}}, \tag{A 16}$$

where the left-hand side operator is

$$\mathscr{L} = \frac{\mathrm{d}^2}{\mathrm{d}y^2} - \left(\frac{2\kappa}{\bar{U}\kappa - \omega}\frac{\mathrm{d}\bar{U}}{\mathrm{d}y} - \frac{1}{\overline{c^2}}\frac{\mathrm{d}\overline{c^2}}{\mathrm{d}y}\right)\frac{\mathrm{d}}{\mathrm{d}y} + \omega^2\left[\frac{(\bar{U}\kappa - 1)^2}{\overline{c^2}} - \kappa^2\right],$$

$\kappa = k/\omega$ and the Fourier transformed source term is

$$\hat{\Gamma}(k, y) = \mathrm{e}^{\mathrm{i}\omega t}\int \Gamma(x, y)\mathrm{e}^{-\mathrm{i}kx}\,\mathrm{d}x.$$

The particular solution to the ordinary differential equation (A 16) can be found in terms of the Green's function $G(y, y_s)$, which is defined by

$$\mathscr{L}G(y, y_s) = \delta(y - y_s). \tag{A 17}$$

Equation (A 17) can be solved numerically as a three-point boundary value problem, using adaptive quadrature to integrate a function $G^-(y, y_s)$ from $y = -\infty$ to a designated matching point y_s, and a function $G^+(y, y_s)$ from $y = +\infty$ to y_s. In the Green's function problem, we replace the Dirac delta function on the right-hand side with the jump conditions at the match point

$$G^+|_{y_s} - G^-|_{y_s} = 0, \quad \left.\frac{\mathrm{d}G^+}{\mathrm{d}y}\right|_{y_s} - \left.\frac{\mathrm{d}G^-}{\mathrm{d}y}\right|_{y_s} = 1 \tag{A 18}$$

and instead solve the homogeneous ODE. The boundary conditions are found by examining (A 17) in the free stream, where the derivatives $\mathrm{d}\bar{U}/\mathrm{d}y$ and $\mathrm{d}\overline{c^2}/\mathrm{d}y$ vanish, resulting in

$$\left[\frac{\mathrm{d}^2}{\mathrm{d}y^2} + \omega^2\left(\frac{(\bar{U}\kappa - 1)^2}{\overline{c^2}} - 1\right)\right]G(y, y_s) = 0.$$

This yields far-field solutions in terms of decaying exponentials, where

$$G(y, y_s) \to \exp\{\mathrm{i}qy\}, \quad \text{as } y \to \pm\infty,$$

the variable q is defined as $q = \omega(\sqrt{(\bar{U}\kappa - 1)^2/\bar{c}^2 - 1})$, and the sign on the square is always chosen to yield a decaying function for G as $y \to \pm\infty$.

Although the numerical solution to (A 17) can be calculated rather quickly for a single matching point y_s, the complete solution for ψ in (A 16) requires $G(y, y_s)$ to be found for many matching points y_s. Fortunately, a reciprocity relation exists for the Green's function at hand

$$\frac{G(y, y_s)}{(\bar{U}(y)k - \omega)^2} = \frac{G(y_s, y)}{(\bar{U}(y_s)k - \omega)^2}, \tag{A 19}$$

and can be used to calculate $G(y_s, y)$ at any y_s once $G(y, y_s)$ is calculated over the y domain (Ray 2006). To obtain the final solution, the convolution integral is used

$$\psi(k, y) = \int_{-\infty}^{\infty} \frac{\mathrm{i}\hat{\Gamma}(k, \xi)}{(\bar{U}(\xi)k - \omega)\,\bar{c}^2} G(y, \xi)\,\mathrm{d}\xi \tag{A 20}$$

to find $\psi(k, y)$ at a particular wavenumber k. To find $\hat{\pi}$ at a specific frequency ω, $\psi(k, y)$ is calculated at a number of points k, and (A 15) is used to transform ψ into (x, y) space.

An additional complication arises in computing the solution to (A 16) and the integral (A 20) when considering the critical layer singularity. For solutions where the mean flow profile $\bar{U}(y)$ and frequency ω cause the term $\bar{U}(y) - \omega$ to vanish, the contour of integration C must be deformed off of the real y-axis to pass over the critical point y_c. Details regarding this procedure are given in Tam & Morris (1980) and the appropriate branch cut for supersonic disturbances of the Rayleigh equation is described in Lin (1955). In addition, the analytic continuation of the mean flow profile $\bar{U}(y)$ must be accounted for, and we use the procedures detailed in Mitchell, Lele & Moin (1999). In a similar fashion, around the critical point y_c, the source term $\Gamma(x, y)$ must be extended into the complex plane to allow the contour deformation to occur in integral (A 20).

REFERENCES

Andersson, P., Henningson, D. S. & Hanifi, A. 1998 On a stabilization procedure for the parabolic stability equations. *J. Engng Math* **33**, 311–332.

Avital, E. J., Sandham, N. D. & Luo, K. H. 1998*a* Mach wave radiations by mixing layers. Part I: Analysis of the sound field. *Theor. Comput. Fluid Dyn.* **12** (2), 73–90.

Avital, E. J., Sandham, N. D. & Luo, K. H. 1998*b* Mach wave radiations by mixing layers. Part II: Analysis of the source field. *Theor. Comput. Fluid Dyn.* **12** (2), 91–108.

Balakumar, P. 1994 Supersonic jet noise prediction and control. Contractor Report to NASA Lewis Research Center, Contract No. NAS3-27205.

Balakumar, P. 1998 Prediction of supersonic jet noise. *AIAA Paper 98-1057*.

Bertolotti, F. P., Herbert, Th. & Spalart, P. R. 1992 Linear and nonlinear stability of the Blasius boundary layer. *J. Fluid Mech.* **242**, 441–474.

Brown, G. L. & Roshko, A. 1974 On density effects and large structure in turbulent mixing layers. *J. Fluid Mech.* **64**, 775–816.

Cheung, L. C. 2007 Aeroacoustic noise prediction and the dynamics of shear layers and jets using the nonlinear PSE. Ph.D. dissertation, Stanford University.

Chu, B. T. 1965 On the energy transfer to small disturbances in fluid flow (Part I). *Acta Mechanica* **1**, 215–234.

Colonius, T., Lele, S. K. & Moin, P. 1997 Sound generation in a mixing layer. *J. Fluid Mech.* **330**, 375–409.

Crighton, D. G. & Gaster, M. 1976 Stability of slowly divergent jet flows. *J. Fluid Mech.* **77**, 397–413.

Day, M. J., Mansour, N. N. & Reynolds, W. C. 2001 Nonlinear stability and structure of compressible reacting mixing layers. *J. Fluid Mech.* **446**, 375–408.

Goldstein, M. E. 2001 An exact form of Lilley's equation with a velocity quadrupole/temperature dipole source term. *J. Fluid Mech.* **443**, 231–236.

Goldstein, M. E. 2003 A generalized acoustic analogy. *J. Fluid Mech.* **488**, 315–333.

Goldstein, M. E. 2005 On identifying the true sources of aerodynamic sound. *J. Fluid Mech.* **526**, 337–347.

Goldstein, M. E. & Leib, S. J. 2005 The role of instability waves in predicting jet noise. *J. Fluid Mech.* **525**, 37–72.

Herbert, T. & Bertolotti, F. P. 1987 Stability analysis of nonparallel boundary layers. *Bull. Am. Phys. Soc.* **32**, 2079.

Ho, C. M. & Huang, L. S. 1982 Subharmonics and vortex merging in mixing layers. *J. Fluid Mech.* **119**, 443–473.

Huerre, P. & Monkewitz, P. A. 1990 Local and global instabilities in spatially developing flows. *Annu. Rev. Fluid Mech.* **22**, 473–537.

Hultgren, L. 1992 Nonlinear spatial equilibration of an externally excited instability wave in a free shear layer. *J. Fluid Mech.* **236**, 635–634.

Jackson, T. L. & Grosch, C. E. 1989 Inviscid spatial stability of a compressible mixing layer. *J. Fluid Mech.* **208**, 609–637.

Laufer, J. & Yen, T. C. 1983 Noise generation by a low Mach-number jet. *J. Fluid Mech.* **134**, 1–31.

Lele, S. K. 1992 Compact finite difference schemes with spectral-like resolution. *J. Comput. Phys.* **103**, 16–42.

Lighthill, M. J. 1952 On sound generated aerodynamically I. General theory. *Proc. Roy. Soc. Lond.* A **222**, 1–32.

Lilley, G. M. 1974 On the noise from jets. AGARD CP-131. 13.1-13.12.

Lin, C. C. 1955 *The Theory of Hydrodynamic Stability*. Cambridge University Press.

Lui, C. C. M. 2003 A numerical investigation of shock-associated noise. Ph.D. dissertation, Stanford University.

Malik, M. R. & Chang, C. L. 2000 Nonparallel and nonlinear stability of supersonic jet flow. *Comput. Fluids* **29** (3), 327–365.

Mitchell, B., Lele, S. K. & Moin, P. 1999 Direct computation of the sound generated by vortex pairing in an axisymmetric jet. *J. Fluid Mech.* **383**, 113–142.

Papamoschou, D. & Roshko, A. 1988 The compressible turbulent shear layer: an experimental study. *J. Fluid Mech.* **197**, 453–477.

Phillips, O. M. 1960 On the generation of sound by supersonic turbulent shear layers. *J. Fluid Mech.* **9**, 1–28.

Ray, P. K. 2006 Sound generated by instability wave/shock-cell interaction in supersonic jets. Ph.D. dissertation, Stanford University.

Rogers, M. M. & Moser, R. D. 1992 The three-dimensional evolution of a plane mixing layer: the Kelvin–Helmholtz rollup. *J. Fluid Mech.* **243**, 183–226.

Sandham, N. D., Morfey, C. L. & Hu, Z. W. 2006 Nonlinear mechanisms of sound generation in a perturbed parallel flow. *J. Fluid Mech.* **565**, 1–23.

Sandham, N. D. & Reynolds, W. C. 1991 Three-dimensional simulations of large eddies in the compressible mixing layer. *J. Fluid Mech.* **224**, 133–158.

Sandham, N. D., Salgado, A. M. & Agarwal, A. 2008 Jet noise from instability mode interactions. *AIAA Paper 2008-2987*.

Schlichting, H., Gersten, K., Krause, E., Oertel, H. Jr. & Mayes, C. 2004 *Boundary Layer Theory*, 8th edn. Springer.

Tam, C. K. W. 1995 Supersonic jet noise. *Annu. Rev. Fluid Mech.* **27**, 17–43.

Tam, C. K. W. & Auriault, L. 1998 Mean flow refraction effects on sound radiated from localized sources in a jet. *J. Fluid Mech.* **370**, 149–174.

Tam, C. K. W. & Burton, D. 1984*a* Sound generation by instability waves of supersonic flows. Part 1. Two dimensional mixing layers. *J. Fluid Mech.* **138**, 249–271.

Tam, C. K. W. & Burton, D. 1984*b* Sound generation by instability waves of supersonic flows. Part 2. Axisymmetric jets. *J. Fluid Mech.* **138**, 273–295.

Tam, C. K. W. & Morris, P. J. 1980 The radiation of sound by the instability waves of a compressible plane turbulent shear layer. *J. Fluid Mech.* **98**, 349–381.

Winant, C. D. & Browand, F. K. 1974 Vortex pairing. *J. Fluid Mech.* **63**, 237–255.

Wu, X. S. 2005 Mach wave radiation of nonlinear evolving supersonic instability modes in shear layers. *J. Fluid Mech.* **523**, 121–159.

Yen, C. C. & Messersmith, N. L. 1998 Application of the parabolized stability equations to the prediction of jet instabilities. *AIAA J.* **36**, 1541–1544.